Graphene edge chemistry and membrane formation with supramolecular approaches using Pt(II)-terpyridine molecular tweezers

Jiao, A.

CHAPTER 5

Influence of fabrication and wettability on the stability and 1/*f* noise in graphene nanopores fabricated by controlled breakdown in NaCl

Graphene nanopores have great potential for biomolecule sequencing applications, but their widespread use is hindered by complex and costly fabrication methods. This study introduces a simple, scalable and reproducible protocol for fabricating single or multiple graphene nanopores using the automated controlled breakdown (CBD) technique. We systematically investigated key fabrication parameters, including the free-standing size of graphene, the influence of sodium dodecyl sulfate (SDS) as an additive, and the multiporosity of the graphene, to better understand the process. Our findings show that smaller free-standing areas of graphene required higher fabrication voltages but resulted in improved pore stability and reduced 1/f noise. Using SDS as an additive could accelerate the fabrication process and enhance the nanopore stability, presumably by increasing the wettability of graphene and preventing residual hydrocarbon adsorption. Finally, hydrophilic surface coatings seemed to either increase or reduce the 1/f noise depending on the graphene nanopore diameter. This work provides a practical, scalable fabrication method and offers critical insights into optimizing graphene nanopore fabrication by controlled breakdown for high-performance applications.

This chapter is based on: *Jiao, A.; Wu, M. Y.; Filippov, D. V.; Bonnet, S.; Schneider, G. F. (in preparation)*

5.1 Introduction

Nanopores are exceptional tools for the characterization of biological macromolecules such as DNA and proteins.[1–3] These devices consist of a pore of nanometer size, either in a protein or a synthetic material like silicon, embedded in an electrically insulating membrane. When a voltage is applied across this membrane, ions will flow through the nanopores if the membrane is submerged in an electrolyte solution. The ionic current is larger for larger pores, but decreases upon pore blockage, for example, when a molecule is traversing the pores. The magnitude of the current blockage depends on the size and structure of the molecules with respect to the nanopore. Specific changes in ionic current (magnitude of blockage, dwell time) give information about traversing molecules, which can be used to differentiate molecules and substructures in biopolymers.[4–7]

State-of-the-art nanopore devices are based on biological nanopores, which consist of a protein nanopore embedded in a lipid bilayer.[8,9] Biological nanopores are used as sequencing devices and are helpful in the field of healthcare for disease prevention, diagnosis and personalized treatment, among other fields such as forensic sciences and agriculture.[3,6,10] While biological nanopores are reproducible and consistent, the disadvantages of biological nanopores are their relative instability and poor resolution due to their thickness.[11] In order to measure single nucleotides, ultrathin nanopores are necessary. Thus, solid-state nanopores are envisioned to be superior to biological nanopores due to the high flexibility of the pore size, shape, thickness and stability.[12] An example of such an ultrathin solid-state nanopore is graphene nanopores, through which DNA translocation has been described in the literature since 2010.[13–15] Unfortunately, graphene-based nanopores suffer from some major fundamental problems, such as high $1/f$ noise,[16] high velocity DNA translocation,[17] clogging tendency,[18] uncontrolled DNA translocation geometry,[19] and poor control of the chemistry around the pore.[19] Moreover, practical problems cannot be neglected as well, such as low yield and reliance on high-end instrumentation, leading to costly and time-consuming fabrication with poor scalability.[20]

To alleviate the time and cost of solid-state nanopore fabrication, controlled breakdown (CBD) has been developed as a simple, scalable method.[21–26] CBD relies on generating defects in the membranes.[27] By applying a potential across this membrane, charge traps will accumulate at the locations of defects, leading to a conductive pathway for electrolytes until the membrane physically breaks down.[28] CBD has been widely explored for SiNx membranes, providing insight on kinetics,[28]

oxidation,[29] stability,[30] influence of pH,[31] charge neutralization,[32] and functionalizability[33,34] of nanopores fabricated in these materials. Few papers report the use of CBD fabricating nanopores in ultrathin materials such as MoS_2,[35] multi-layer graphene,[36–38] and single-layer graphene membranes.[36,39] The preparation of nanopores in ultrathin materials is more time-consuming, as 2D materials are not sufficiently stable without a substrate and must be transferred or grown on an existing, prefabricated solid-state nanopore.[27] Moreover, automation of the CBD process could accelerate the fabrication of these nanopores. While automated CBD in SiNx membranes has been developed, these methods are yet to be tested on 2D materials.[40,41]

Since CBD is performed in salt solutions, the type and concentration of electrolyte can influence the CBD process. For example, increased electrolyte concentration can result in decreased pore size formation in thermoplastic materials.[42] Additionally, LiCl buffers can accelerate fabrication and improve stability of SiNx nanopores compared to KCl buffers.[40,43] These enhanced fabrication and stability were attributed to better wetting properties of LiCl.[43] Understanding the influence of electrolyte on other materials such as graphene could improve the efficiency and reliability of graphene nanopore fabrication. While LiCl and KCl are commonly reported for CBD,[21,22,28,31,36,39–41,44–48] NaCl remains less frequently investigated.[40,49] In this work, we introduce a simple, scalable and automated controlled breakdown protocol for graphene nanopore fabrication in NaCl. Fabrication parameters, including applied voltage, solution conditions, and free-standing area of graphene, were investigated for their influence on pore formation, stability, and noise characteristics. Furthermore, to study the influence of wettability on graphene nanopore fabrication, we have investigated the influence of sodium dodecyl sulfate (SDS) on the fabrication efficiency and stability of these nanopores.

5.2 Results and Discussion

5.2.1 Graphene membrane preparation

Our graphene samples consisted of single-crystal CVD graphene transferred on commercial SiNx chips with 100 nm or 500 nm apertures obtained from Norcada (Figure 5.1A). To prevent delamination of the graphene, SiNx chips were first functionalized with a pyrene adhesion layer according to Kang et al.[50] This pyrene adhesion layer was applied by a two-step reaction of hydroxyl groups on the surface with 3-aminopropyl-triethoxysilane (APTES) followed by 1-pyrenebutyric acid. Contact angle measurements revealed contact angles of 42.2 ± 8.8° and 69.6 ± 10.2° after APTES and pyrene functionalization, respectively, demonstrating successful coating of the SiNx surface (Figure S5.1). Graphene was then transferred by PMMA-assisted wet transfer method according to Kang et al.[50] After removal of the polymer, the sample was annealed at 80 °C to improve adhesion of the graphene to the substrate and minimize the leakage current. More details of the sample preparation can be found in the Supplementary Information. Optical microscopy showed that the graphene was successfully transferred on the chip (Figure 5.1B). For graphene transferred onto 500 nm aperture SiNx chips, the quality of the graphene could be confirmed by Raman spectroscopy, demonstrating the presence of the signature 2D and G peaks at 2677 cm^{-1} and 1587 cm^{-1}, respectively (Figure 5.1C). The absence of D peak indicates minimal defects in the graphene.

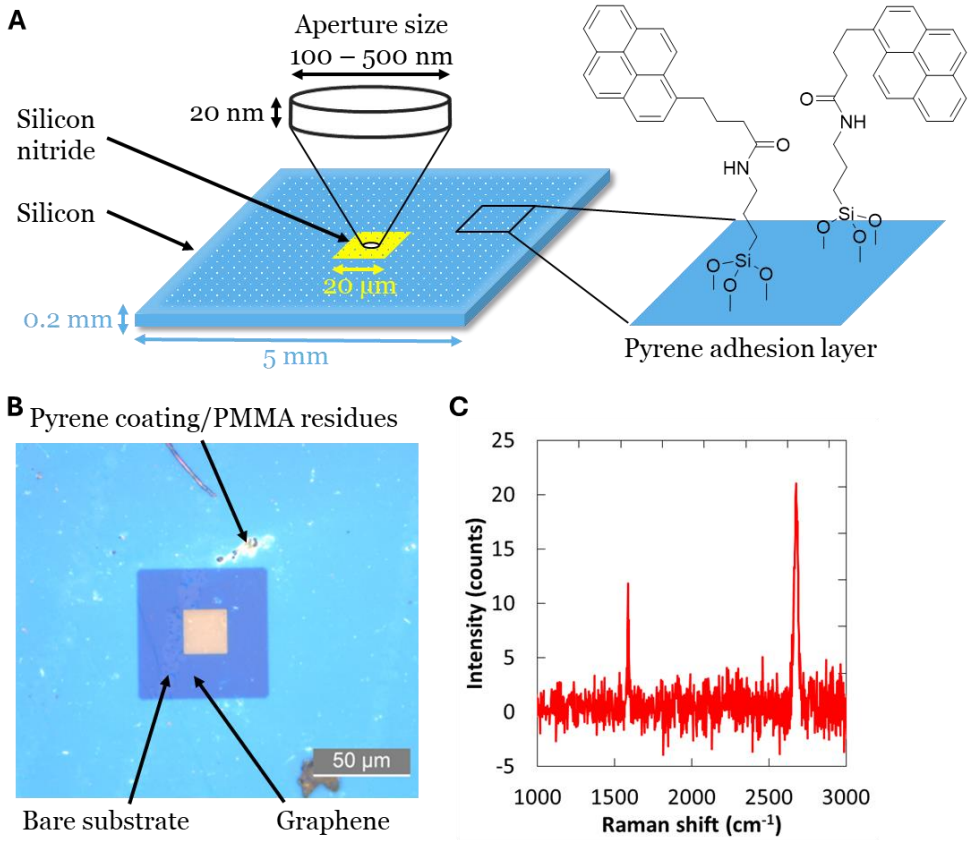

Figure 5.1 Graphene membrane platform for controlled breakdown. (A) Illustration of the graphene sample. Graphene was transferred on top of a chip containing a 100 or 500 nm aperture in a 20 nm thick SiNx membrane. The SiNx chip was first functionalized with a pyrene adhesion layer before graphene transfer. (B) Optical image of graphene transferred on top of the SiNx chip. The apertures were located in the center of the 20 nm thick SiNx membranes, which could be observed as yellow squares. (C) Raman spectrum after background subtraction of free-standing graphene was measured with a green laser (532 nm, 2 mW).

5.2.2 Graphene nanopore fabrication by controlled breakdown

Graphene nanopore fabrication by controlled breakdown (CBD) has been reported before. Kuan et al.[39] have demonstrated nanopore fabrication in CVD graphene using KCl solution. Their strategy entailed manual pulse triggering using 250 ns pulses of 5 – 7 V to fabricate single graphene nanopores.[39] In another study, Guo et al.[36] have demonstrated nanopore fabrication in exfoliated graphene in KCl solutions. Due to the high quality of exfoliated graphene, their strategy combined CBD with artificial

surface defect generation by plasma etching and laser irradiation to generate highly stable graphene nanopores.[36] In this work, nanopore fabrication in CVD graphene was studied using NaCl solutions following a protocol for CBD similar to the one described by Waugh et al.[41] Our graphene-transferred SiNx chips were mounted in commercial fluidic cells purchased from Northern Nanopore Instruments (NNi) (part of Oxford Nanopore Technologies (ONT) since November 2023) (Figure 5.2A). Graphene nanopore fabrication was performed in two steps and was adapted from protocols initially optimized for the fabrication of single nanopores in SiNx membranes. The fabrication process comprises two steps: pore nucleation and pore enlargement (Figure 5.2B and Figure 5.2C, respectively).[41] This protocol was optimized to ensure that only a single pore was formed during the pore nucleation step by carefully controlling the voltage until a sharp increase in current was observed, indicating pore formation.[41] Afterwards, to prevent additional pore formation during the pore enlargement step, a lower voltage than the voltage used during the previous nucleation step was used.[41]

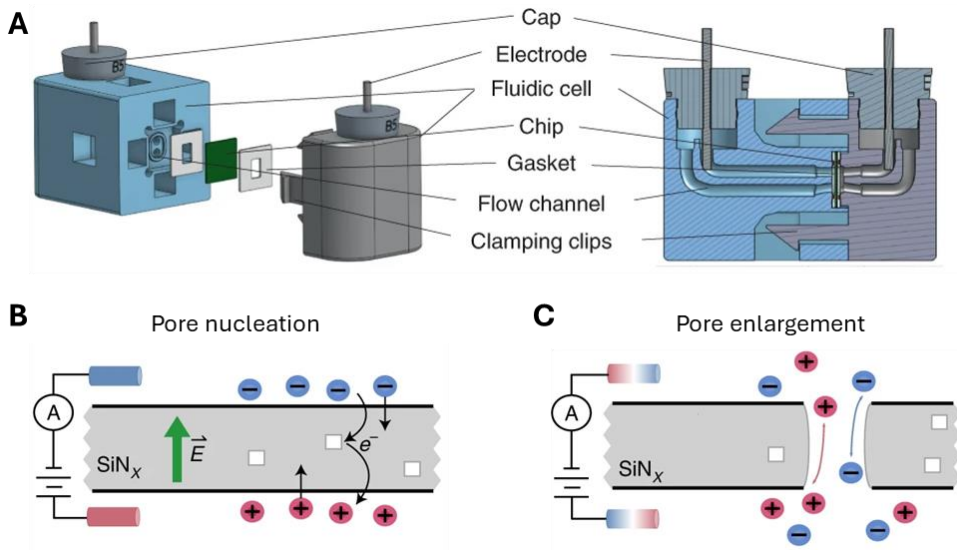

Figure 5.2 The fluidic cell for and the mechanism of controlled breakdown. (A) Illustration of the different components in the fluidic cell used to perform controlled breakdown. On the left is depicted an expanded view, and on the right is depicted a side profile of the fluidic cell. (B) Illustration of pore nucleation in a SiNx membrane. A constant voltage is applied over the membrane, resulting in buildup of defects until the membrane breaks down. (C) Illustration depicting the process of pore enlargement in a SiNx membrane. Successive pulses of alternating voltage were applied to enlarge the pore. Figure is reproduced from Waugh et al.[41]

After mounting the chips in the fluidic cells, the graphene membranes were wetted by carefully flushing isopropanol through the chambers of the fluidic cells. Then, the solution was replaced with aqueous NaCl (10 mM 4-(2-hydroxyethyl)-1-piperazineethanesulfonic acid (HEPES), titrated with NaOH to pH 8). Before initiating graphene nanopore fabrication, the current-voltage (I-V) measurements were recorded to confirm the absence of leakage ($G < 0.3$ nS) (blue triangles in Figure S5.2A). Pore nucleation was performed by applying a voltage ramp until a sudden increase in current was monitored, after which the system automatically terminated the nucleation process (Figure 5.3A). The I-V curve was then measured again to confirm an increase in conductance, indicative of pore formation (red squares in Figure S5.2A). Pore enlargement was performed by applying blocks of short pulse cycles of alternating voltage (red blocks in Figure 5.3B). The magnitude of the voltage for this enlargement step was chosen as a percentage of the breakdown voltage of the same sample to minimize the formation of additional pores. In general, we started enlarging at 50% of the breakdown voltage, and this voltage was increased in steps of 10% if no significant enlargement was observed (Figure 5.3C). This process was continued until a target conductance was reached, after which the system automatically terminated the enlargement process (Figure 5.3D). The enlargement process was monitored by taking quick conductance measurements called “quick measures”, which extracts the conductance from the current values measured at +100 mV and -100 mV (Figure S5.3). These quick measures were performed in between blocks of pulse cycles (green blocks in Figure 5.3B). The final pore size was calculated from I-V measurements (black dots in Figure S5.3B). Additional details on graphene nanopore fabrication can be found in the methods section.

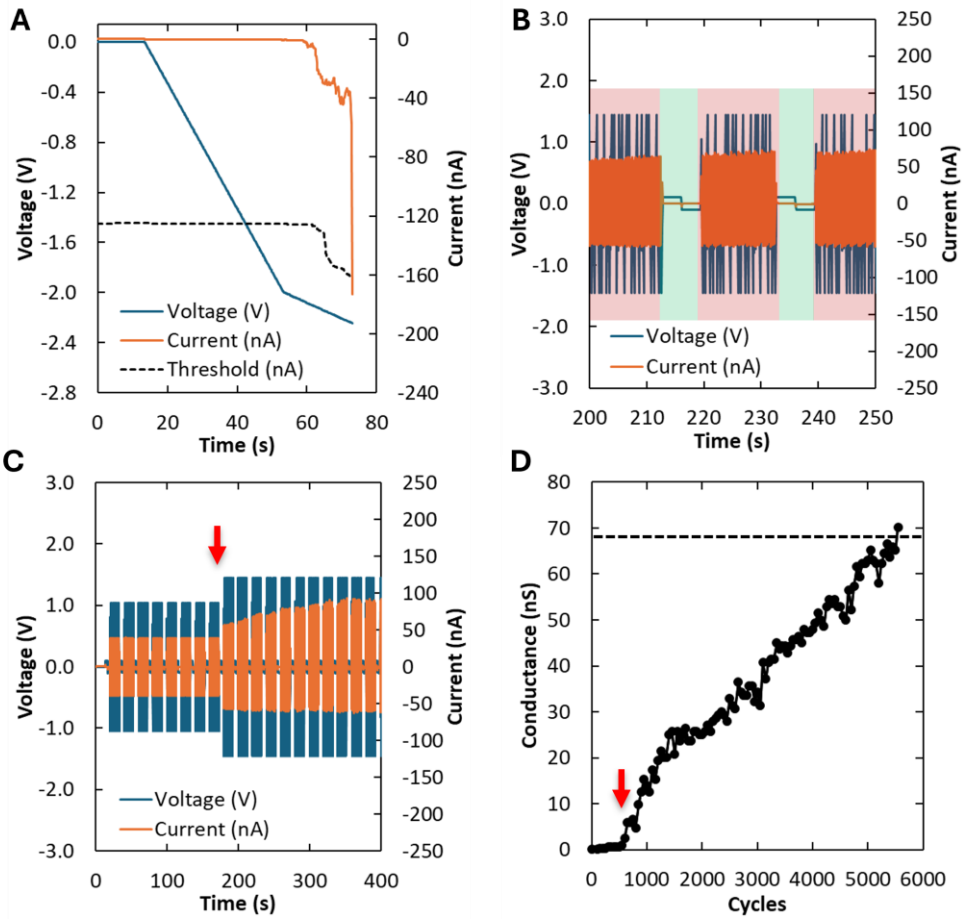

Figure 5.3 Process of pore nucleation and pore enlargement in a free-standing graphene film on a SiNx chip with 100 nm aperture diameter (sample 2). (A) Pore nucleation was accomplished in 3.6 M NaCl + 10 mM HEPES by ramping the voltage (blue trace) until a sudden increase in current (orange trace) at 2.2 V exceeded a set threshold (black dashed trace). (B) Pore enlargement was accomplished in 1.0 M NaCl + 10 mM HEPES by cycling blocks of short pulses (50 × 0.1 s) of applied voltage alternating from +1.46 V to -1.46 (red blocks). To monitor the enlargement process, "quick measures" were performed in between blocks of pulse cycles (green blocks), which extracts the conductance from the current values measured at +100 mV and -100 mV. (C) Since the measured conductance during the enlargement process did not increase significantly after 8 blocks of pulse cycles at applied voltages of ±1.00 V, the applied voltage was increased (red arrow) to ±1.46 V to speed up pore enlargement. (D) The enlargement process was continued until a target conductance of 67 nS (dashed line) was reached, which corresponds to a single graphene nanopore with a diameter of 10 nm according to Equation (1) in 1.0 M NaCl + 10 mM HEPES.

Controlled breakdown protocol optimization

Several problems were occasionally encountered during the pore nucleation and pore enlargement processes. First, pore nucleation sometimes did not occur even at high applied potentials of -10 V (Figure S5.4A). The absence of pore nucleation can be explained by the sample contamination, such as PMMA residues or other large particles blocking the graphene. Second, during the pore nucleation process, a sharp decrease in the absolute current was sometimes observed while ramping up the voltage. The sharp decrease was often followed by a sharp increase in the absolute current, which led to premature breakdown events (Figure S5.4B). Third, during the pore nucleation process, sometimes insufficient conductance values ($G < 0.3$ nS) were measured after detection of a breakdown event (Figure S5.4C). These false breakdown events could be explained by voltage-mediated delamination (VMD), which is a reversible phenomenon that allows ions to bypass the graphene membrane only under high applied potential (Figure S5.5A).[51] Because VMD is reversible and depends on the applied potential, these large conductance values measured at high applied potentials during the pore nucleation process (>1 V) will rapidly drop to insignificant conductance values at low applied potentials of ≤100 mV used for I-V measurements. Interestingly, continuation with pore enlargement after false breakdown sometimes still led to enlargement of the pore (Figure S5.4D), suggesting that pore nucleation was not strictly necessary for graphene nanopore fabrication. Finally, the pore nucleation process occasionally resulted in excessive conductance after detection of a breakdown event equivalent to pore diameters of 15 – 100 nm. Such events can be attributed to overdue breakdown termination and damage to the graphene membrane. To minimize false and excessive breakdown events, we optimized the offset threshold in the current at which the system detects the breakdown event. False breakdown events were common when an offset of 25 nA was applied, while excessive breakdown was common when an offset of 250 nA was applied. Consequently, an offset of 125 nA was generally applied to achieve the best balance and ensure reliable pore nucleation.

Several types of problems were encountered during the pore enlargement process. First, a sudden increase or decrease in conductance was occasionally observed during enlargement, which results from damaging or clogging of the graphene membrane (Figure S5.5B). Second, the measured conductance during the enlargement process was often overestimated, leading to an apparent instability in pore conductance (Figure S5.5C). We hypothesize that this instability in measured conductance was due to VMD, since this apparent instability disappeared by waiting for several minutes before measuring the conductance again. Alternatively, this

phenomenon can be a consequence of charging during the conditioning. In this case, the problem could be solved by, for example, applying surface coating modifications.[52] To minimize this instability in measured pore conductance without external modifications, we tested changes in the waiting time and pulse durations. While longer waiting times of 5 – 120 s reduced the probability of conductance overestimation, they drastically increased the total nanopore fabrication time. Therefore, a waiting time of 1 s was chosen to maintain a scalable process. Next to varying the waiting time, decreasing the pulse duration from 1 s to 0.1 s also reduced the probability of conductance overestimation. Since shortening the pulse duration slowed down the pore enlargement process and increased the number of quick measures (green blocks in Figure 5.3B) before reaching the target conductance, the number of pulses between quick measures was increased from 5 to 50. Finally, some pores failed to enlarge or enlarged very slowly even when voltages were increased from 50% to 100% of the apparent nucleation voltages (Figure S5.5D). Failure to enlarge the pores can be explained by the absence of an actual pore, where the measured conductance originated from leakage or VMD. In these cases, returning to the pore nucleation process sometimes remedied this problem.

In this study, we generally targeted pores with diameters of 5 or 10 nm. As a result of the aforementioned problems, we sometimes obtained pores that would exceed the conductance that we expected. For example, pore nucleation resulting in excessive conductance values indicated membrane damage rather than single-pore fabrication. Therefore, for the purpose of analyzing the pore nucleation, we only included breakdown events resulting in conductance values equivalent to single cylindrical pore diameters smaller than 3 nm (length of 24 carbon-carbon bonds in a graphene lattice). To analyze the pore enlargement, we only included stable enlargement events resulting in conductance values equivalent to single cylindrical pore diameters between 4 – 15 nm. The relation between pore conductance and the diameter of a single cylindrical nanopore is given in equation (1):

$$(1) \quad G = \sigma \left(\frac{4T}{\pi d^2} + \frac{1}{d} \right)^{-1},$$

where G is the experimental conductance (in S), σ is the bulk conductivity of the solution (in S m^{-1}), T is the thickness of the membrane (in m), and d is the diameter of the nanopore (in m).[53]

Influence of 1.0 M vs 3.6 M NaCl on CBD

First, we investigated the effect of the NaCl concentration on nucleation voltage and success rate in SiNx chips with an open-pore aperture of 100 nm in diameter. Note that all buffer solutions used throughout this study contain 10 mM HEPES (see methods section). The full list of results are provided in Table S5.1 and Table S5.2. An average nucleation voltage ± standard error (SE) of 3.6 ± 0.3 V (N = 6) was needed to nucleate a pore in 3.6 M NaCl (blue squares in Figure 5.4A). Similar values of 2.9 ± 0.7 V (N = 3) were found when a lower concentration of 1.0 M NaCl was used instead ($p = 0.39$, see methods section) (orange diamonds in Figure 5.4A). Furthermore, the average nucleated pore diameter (± SE) in 3.6 M NaCl was 1.3 ± 0.4 nm, which was similar to the average nucleated pore diameter of 1.2 ± 0.7 nm in 1.0 M NaCl ($p = 0.80$). These results suggest that the difference in concentration between 1.0 M NaCl and 3.6 M NaCl does not significantly influence the average nucleation voltage and the nucleated pore size. However, more practical difficulties were encountered during pore nucleation in 1.0 M NaCl than in 3.6 M NaCl. In 1.0 M NaCl, most samples resulted in either false breakdown (insignificant conductance after breakdown) or no breakdown events, even at high a potential of 10 V. Good reproducibility was found for pore nucleation in 3.6 M NaCl, possibly due to the higher ionic strength. Therefore, we generally continued using 3.6 M NaCl for pore nucleation.

After pore nucleation, we investigated the influence of the NaCl concentration on the enlargement voltage and enlargement efficiency in SiNx chips with 100 nm aperture diameters. The results are listed in

Table S5.3 and Table S5.4. In 3.6 M NaCl, the voltage (± SE) needed to be increased to 2.30 ± 0.05 V (N = 2) (blue squares in Figure 5.4B) before the pores started to enlarge. Similar enlargement voltages of 2.2 ± 0.3 V (N = 6) were found in 1.0 M NaCl (p = 0.65) (orange diamonds in Figure 5.4B). The number of cycles (± SE) needed to increase the conductance equivalent to increasing the diameter of a single graphene nanopore by 1 nm in 3.6 M NaCl was 1.2 ± 1.0 × 10^3 cycles nm^{-1}. The number of cycles per nm enlargement found in 1.0 M NaCl was similar (4.6 ± 1.7 × 10^2 cycles nm^{-1}) (p = 0.50). From these results, it could not be concluded whether the difference in NaCl concentration significantly influenced the enlargement voltage and enlargement efficiency. Larger differences in concentration may result in significant variations in controlled breakdown parameters.[44]

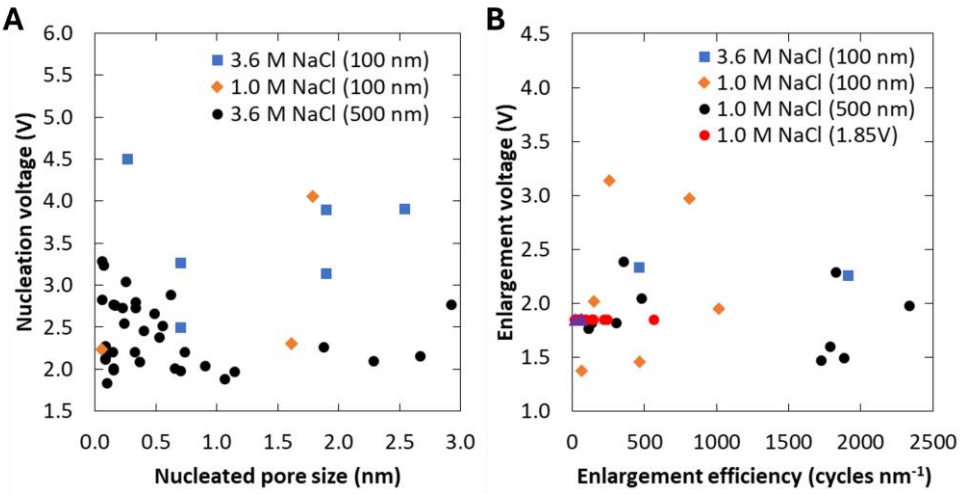

Figure 5.4 Influence of NaCl concentration and aperture diameters of SiNx chips on nanopore fabrication by controlled breakdown. (A) Scatter plot of nucleation voltage (in V) and their respective nucleated pore sizes (in nm). (B) Scatter plot of enlargement voltage (in V) and their respective enlargement efficiencies (in cycles nm^{-1}). Blue squares represent samples fabricated in 3.6 M NaCl + 10 mM HEPES on SiNx chips with 100 nm aperture diameters. Orange diamonds represent samples fabricated in 1.0 M NaCl + 10 mM HEPES on SiNx chips with 100 nm aperture diameters. Black dots represent samples fabricated in 3.6 M NaCl + 10 mM HEPES in panel A and 1.0 M NaCl + 10 mM HEPES in panel B on SiNx chips with 500 nm aperture diameters. Red dots represent samples fabricated in 1.0 M NaCl + 10 mM HEPES on SiNx chips with 500 nm aperture diameters using static enlargement voltages of 1.85 V.

Influence of the size of free-standing graphene on CBD

To examine how the size of the free-standing part of graphene affects controlled breakdown, graphene was transferred onto SiNx chips with aperture sizes of 100 nm and 500 nm. When using SiNx chips with 500 nm aperture diameter, the average nucleation voltage for pore nucleation in 3.6 M NaCl was 2.4 ± 0.1 V (N = 36) (black dots in Figure 5.4A). This value was significantly lower than the average nucleation voltage of 3.5 ± 0.3 V when using SiNx chips with 100 nm aperture diameter ($p = 0.01$). The lower nucleation voltage observed with 500 nm chips could be explained by a higher probability of defects in larger apertures, which increases the likelihood of pore nucleation at lower nucleation voltages. Furthermore, the average nucleated pore size was found to be 0.6 ± 0.1 nm, which was slightly lower than the average nucleated pore size found in SiNx chips with 100 nm aperture diameter (1.3 ± 0.4 nm) ($p = 0.10$).

For pore enlargement in SiNx chips with 500 nm aperture diameter, the average minimal enlargement voltage in 1.0 M NaCl was 1.9 ± 0.1 V (black dots in Figure 5.4B) (N = 10), which was similar to the average value found in 100 nm chips (2.2 ± 0.3 V) ($p = 0.41$). The enlargement efficiency in SiNx chips with 500 nm aperture diameter was $1.1 \pm 0.3 \times 10^3$ cycles nm^{-1}, which was slightly lower than in SiNx chips with 100 nm aperture diameter ($4.6 \pm 1.7 \times 10^2$ cycles nm^{-1}) ($p = 0.07$). In conclusion, the pore nucleation and enlargement processes were augmented by larger free-standing graphene areas, suggesting that the controlled breakdown process is a stochastic process, as larger free-standing areas offer more opportunities to grow and enlarge pores. Since nucleated pore sizes of 0.5 ± 0.3 nm were demonstrated to produce single graphene nanopores,[39] we generally used SiNx chips with 500 nm aperture diameter for further studies, since this platform seemed to produce pores more weighted towards these sizes. An additional advantage of using SiNx chips with 500 nm aperture diameter was the possibility of characterizing the free-standing graphene using Raman spectroscopy.

Influence of enlargement voltage on CBD

To investigate whether the applied enlargement voltage could affect enlargement efficiency, enlargement in 1.0 M NaCl was monitored on SiNx chips with a 500 nm aperture diameter with a static enlargement voltage applied, regardless of the nucleation voltage (red dots in Figure 5.4B). For the static enlargement voltage, a value close to the average value for 1.0 M NaCl was chosen, which was 1.85 V. For several samples, 1.85 V was either not large enough to enlarge the pores, or the enlargement process led to overshooting of the target pore diameters. Most samples were enlarged at a controlled speed when an enlargement voltage of 1.85 V was

applied. The corresponding average enlargement efficiency was $1.2 \pm 0.4 \times 10^2$ cycles nm^{-1} (N = 15), which was significantly lower than the enlargement efficiency measured previously at minimal enlargement voltages ($1.1 \pm 0.3 \times 10^3$ cycles nm^{-1}) (p = 0.01). An explanation for this difference in enlargement efficiency could be that the enlargement voltage of 1.85 V was, on average, higher than the minimum enlargement voltage required for these samples. Therefore, we conclude that the enlargement efficiency was voltage-dependent, and increasing the enlargement voltage could accelerate the enlargement process.

Influence of SDS on CBD

To investigate the influence of SDS on CBD, we performed pore nucleation and pore enlargement in 1.0 M NaCl + 10 μM SDS and 3.6 M NaCl + 10 μM SDS solutions. In the presence of SDS, the average nucleation voltages were similar at 2.44 ± 0.18 V (N = 5) and 2.62 ± 0.34 V (N = 2) in 1.0 M NaCl + 10 μM SDS (green triangles in Figure 5.5A) and 3.6 M NaCl + 10 μM SDS (yellow crosses in Figure 5.5A), respectively. These values were also similar to the average nucleation voltage found in 3.6 M NaCl without SDS (2.40 ± 0.07 V) (p = 0.52 – 0.80), suggesting that SDS did not influence the nucleation voltage. Average nucleated pore sizes of 0.25 ± 0.14 nm and 0.20 ± 0.05 nm were found in 1.0 M + 10 μM SDS and 3.6 M NaCl + 10 μM SDS, respectively. These values were slightly lower than the average nucleated pore size found in 3.6 M NaCl without SDS (0.56 ± 0.12 nm) (p = 0.001 – 0.07), though it cannot be excluded that the SDS adsorption around small graphene nanopores could influence the conductance measurements.[54]

Significant differences were observed in pore enlargement when SDS was present. The minimal enlargement voltage in 1.0 M NaCl + 10 μM SDS was 1.50 ± 0.04 V (N = 3) (green triangles in Figure 5.5B), which was significantly lower than the enlargement voltage found in 1.0 M NaCl without SDS (1.86 ± 0.12 V) (p = 0.005) (black dots in Figure 5.5B). At these respective voltages, the enlargement efficiency found in 1.0 M NaCl + 10 μM SDS was $2.3 \pm 1.5 \times 10^2$ cycles nm^{-1}, which was significantly lower than the enlargement efficiency found in 1.0 M NaCl without SDS ($1.1 \pm 0.3 \times 10^3$ cycles nm^{-1}) (p = 0.02). When a static enlargement voltage of 1.85 V was applied, the enlargement efficiency in 1.0 M NaCl + 10 μM SDS was 46 ± 18 cycles nm^{-1} (N = 3) (purple triangles in Figure 5.5B), which was slightly lower compared to the enlargement efficiency in 1.0 M NaCl without SDS ($1.2 \pm 0.4 \times 10^3$ cycles nm^{-1}) (p = 0.08) (red dots in Figure 5.5B). From these results, we conclude that the presence of SDS accelerates pore enlargement in graphene by lowering the enlargement voltage barrier and enhancing the enlargement efficiency, presumably by increasing the wettability of graphene.

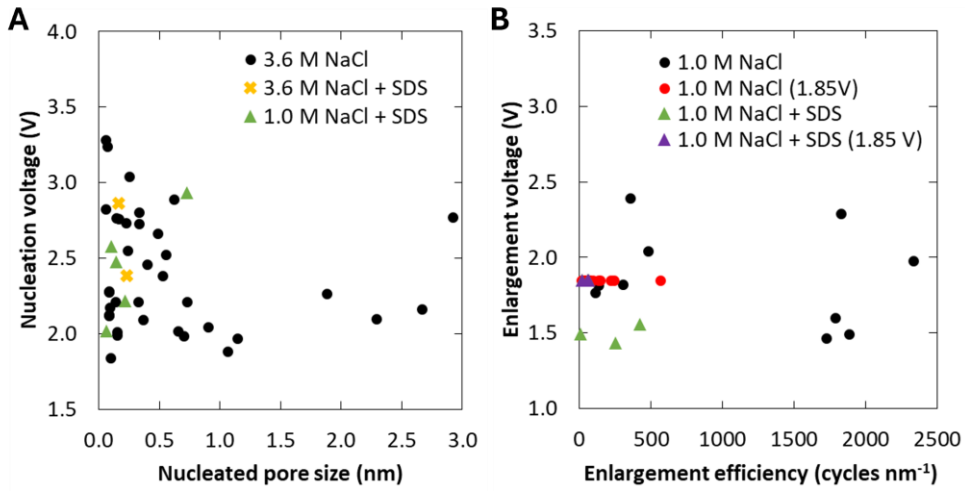

Figure 5.5 Influence of sodium dodecyl sulfate (SDS) on graphene nanopore fabrication by controlled breakdown on SiNx chips with 500 nm aperture diameters. (A) Scatter plot of nucleation voltage (in V) and their respective nucleated pore sizes (in nm). (B) Scatter plot of enlargement voltage (in V) and their respective enlargement efficiencies (in cycles nm^{-1}). Black dots represent samples fabricated in 3.6 M NaCl + 10 mM HEPES in panel A and 1.0 M NaCl + 10 mM HEPES in panel B. Yellow crosses represent samples fabricated in 3.6 M NaCl + 10 mM HEPES + 10 µM SDS. Green triangles represent samples fabricated in 1.0 M NaCl + 10 mM HEPES + 10 µM SDS. Red dots represent samples fabricated in 1.0 M NaCl + 10 mM HEPES using static enlargement voltages of 1.85 V. Purple triangles represent samples fabricated in 1.0 M NaCl + 10 mM HEPES + 10 µM SDS using static enlargement voltages of 1.85 V.

5.2.3 Multiporosity of the graphene nanopores fabricated by CBD

Following controlled breakdown, the nanopores were characterized by measuring the pore conductance. While the size of a single cylindrical nanopore can be estimated from Equation (1),[53] the experimental conductance cannot determine the number of nanopores that have been fabricated. To determine the number of nanopores in the graphene, the graphene was functionalized with a pyrene-polyethylene glycol (PPEG) coating (Figure 5.6A).[18] This coating consists of an adsorbed monolayer of 1-aminopyrene reacted with the m-PEG_4-NHS ester to form a hydrophilic surface provided by the protruding polyethylene glycol moieties.[18] Upon applying this coating on the graphene membrane, the coating will obstruct the pore and thereby decrease the measured conductance. The influence of this coating on the pore conductance has been reported before according to the following Equation (2):

$$(2) \quad G' = \sigma \left(\frac{4(T+2L)}{\pi(d-2\Delta R)^2} + \frac{1}{d-2\Delta R} \right)^{-1},$$

where *G'* is the conductance of the coated nanopore (in S), L is the effective increase in membrane thickness (in m), and ΔR is the effective decrease in nanopore diameter due to the coating (in m).[18,39] Using the same values for ΔR and L as Kuan et al.[39], we found that the conductance values for most samples upon pore coating were different than expected for single pores (Figure 5.6B). One sample exhibited a new conductance value close to the expected value for a single nanopore, while three other data points fitted better to the simulated curves for 4 to 23 pores (assuming equally sized, independent pores). Interestingly, one sample exhibited an insignificant change in conductance after PPEG coating. This anomaly could be explained by either unsuccessful coating of the pore, or a simultaneous unclogging/damage event resulting in the PPEG coating being masked by the increase in conductance from unclogging/damage. Unclogging/damage could occur during manipulation and rinsing of the sample during the PPEG coating procedure. These results therefore suggest that the CBD protocol described in this work can result in the formation of single and multiple nanopores.

Next to PPEG coating experiments, we also characterized graphene nanopores using transmission electron microscopy (TEM). When using TEM with an acceleration voltage of 80 kV, the graphene membrane seemed intact with no holes to be observed (Figure S5.6A-C). During the measurement, we also observed carbon contamination due to electron beam exposure. Therefore, it may be possible that small holes became sealed due to carbon contamination, which could explain the absence of observed nanopores. At 300 kV acceleration voltage, micropores started to form during electron beam exposure due to electron beam damage, which complicated the analysis (Figure S5.6D-F). Interestingly, after formation of the micropores during TEM at 300 kV, prolonged electron beam exposure did not form new pores other than enlarging present pores. Absence of continuous pore formation suggests that pores cannot be formed spontaneously by prolonged electron beam exposure. We hypothesize that the observed micropores were enlarged from nanopores or defects fabricated by CBD due to increased reactivity of graphene edges. The fact that multiple micropores were formed during TEM suggests that multiple nanopores may have been fabricated during CBD, though it cannot be excluded that existing defects before nanopore fabrication may play a role.

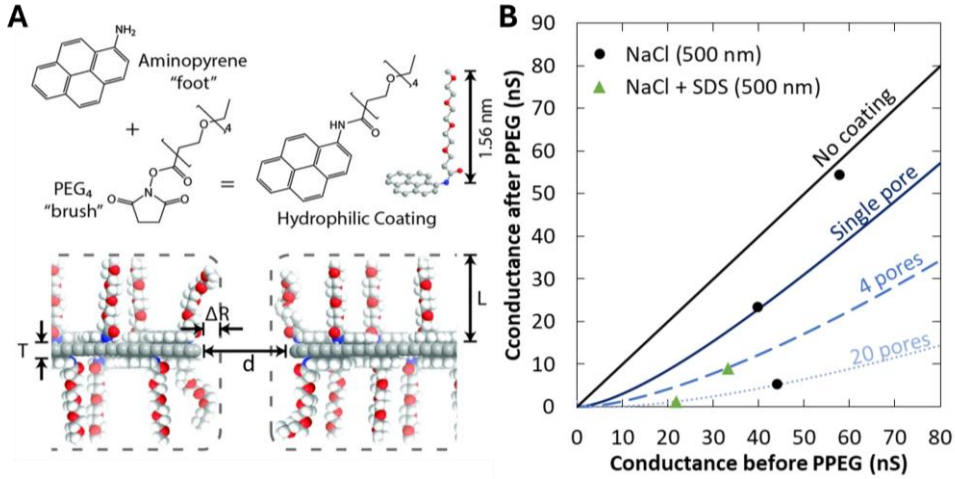

Figure 5.6 Characterization of graphene nanopores after coating with pyrene-polyethylene glycol (PPEG) or sodium dodecyl sulfate (SDS). (A) Illustration of a graphene nanopore functionalized with the PPEG coating. Figure reproduced from Kuan et al.[39] (B) Conductance (in nS) of graphene nanopores fabricated on SiNx chips with 500 nm aperture diameter measured in 1.0 M NaCl + 10 mM HEPES before coating (x-axis) and after coating (y-axis) with PPEG. The results are listed in Table S5.5. Black dots represent samples fabricated without the presence of SDS. Green triangles represent samples fabricated in the presence of SDS.

5

5.2.4 Stability of graphene nanopores fabricated by CBD

The stability of biological and solid-state nanopores are generally limited to several hours.[36,55,56] In the case of graphene nanopores, changes in nanopore conductance can be observed immediately after fabrication.[30,36] Graphene is notorious for surface contamination problems,[57] and many molecules such as polymer residues from graphene transfer methods[58] and airborne hydrocarbons[59,60] can non-covalently stick to graphene, which can lead to clogging of graphene nanopores. Moreover, graphene nanopores can seal themselves under electron beam irradiation when carbon sources are present, also known as self-healing.[61–63] In such cases, passivation of the graphene edges with Si atoms can improve graphene nanopore stability.[64] Similarly, passivation of graphene edges with ascorbic acid can improve graphene nanopore stability to survive harsh conditions such as concentrated sodium persulfate and sulfuric acid solutions.[65] In this study, graphene nanopore stability was investigated over time in NaCl solutions with and without SDS and after flushing with NaCl solutions with and without SDS. The aperture diameter of the SiNx chips, NaCl concentration and presence of SDS were investigated as possible factors for nanopore stability.

Nanopore stability over time

Immediately after the process of pore enlargement, the conductance of graphene nanopores were monitored in 1.0 M and 3.6 M NaCl solutions with and without SDS over time (Figure 5.7A). The pore stability was defined by the change in conductance over time. For graphene nanopore sample **6** on a SiNx chip with 100 nm aperture diameter, an initial conductance of 68 nS was measured in 1.0 M NaCl after finishing pore nucleation and pore enlargement. The pore conductance was then measured every 30 s over the next 10 min, which ranged from 67 – 69 nS in 1.0 M NaCl (orange diamonds in Figure 5.7A). The small differences in conductance values suggest that the pore was exceptionally stable over 10 min in 1.0 M NaCl with changes <2% in conductance (N = 1) (orange diamonds in Figure 5.7B). For graphene nanopores on SiNx chips with 500 nm aperture diameter, the pore stability was monitored in 1.0 M NaCl (N = 7) and 3.6 M NaCl (N = 3) (black and blue dots, respectively, in Figure 5.7). Out of these 10 samples, 5 samples remained stable with <10% changes over 10 min, while the other 5 samples showed a steady decrease in conductance up to 29% after 10 min. The largest changes were found in the first few minutes after fabrication, though the conductance continued to decrease by up to 38% after 2 h (Figure 5.7B). This behavior is similar to graphene nanopores fabricated by TEM drilling.[30] The decrease can be explained by clogging of the graphene nanopore by residual hydrocarbon contamination in the solution. While VMD in graphene on SiNx chips with 50 nm aperture diameter was reported to occur on the seconds (s) timescale,[51] it cannot be excluded that VMD could play a role over longer periods of time in these particular samples, where SiNx chips contained larger aperture diameters of 500 nm and were functionalized with a pyrene adhesion layer. It is worth noting that for sample **55** fabricated without any enlargement, the conductance increased from 171 nS to 197 nS in 3.6 M NaCl over 20 min after fabrication (red crosses in Figure 5.7). This was the only sample for which an increase in conductance was observed over time instead of a decrease, suggesting that pore stability may be fabrication-dependent.

To investigate whether SDS could influence the pore stability over time, the conductance of graphene nanopores fabricated on SiNx chips with 500 nm aperture diameter after enlargement in 1.0 M NaCl + 10 μM SDS were monitored over time in the same solution (N = 2) (green triangles in Figure 5.7). No significant difference in stability could be observed within the first 20 minutes in 1.0 M NaCl + 10 μM SDS compared to NaCl solutions without SDS (Figure 5.7A). Interestingly, only a slight decrease in conductance from 100 nS to 94 nS was measured over a longer period of 2 h in 1.0 M NaCl + 10 μM SDS (N = 1). This change in conductance did

not exceed 10% (Figure 5.7B), suggesting that SDS may improve the long-term stability of the nanopore, possibly by solvation of residual hydrocarbons and preventing adsorption to graphene.

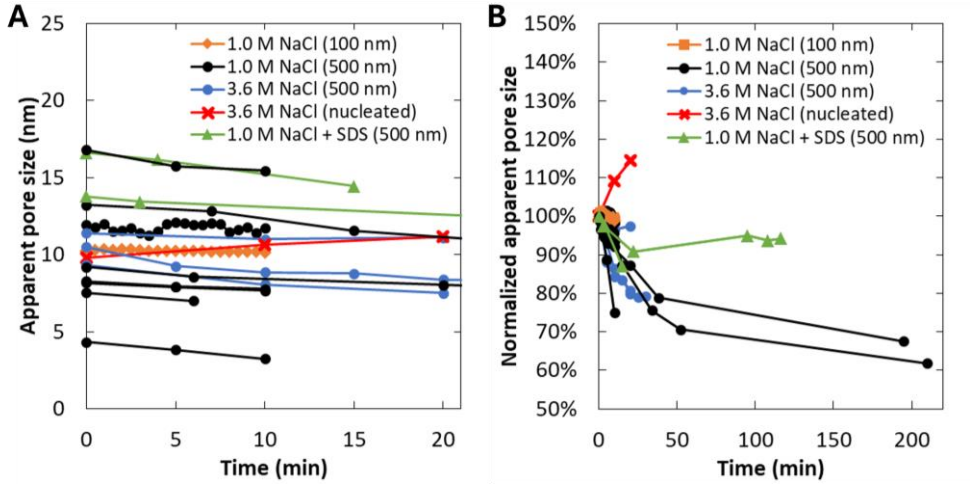

Figure 5.7 Graphene nanopore stability over time in NaCl solutions with and without SDS. (A) Conductance (in nS) of graphene nanopores on SiNx chips in NaCl solutions over time in the first 20 minutes after nanopore fabrication. (B) Normalized conductance of graphene nanopores on SiNx chips in NaCl solutions over time up to 210 minutes after nanopore fabrication. The results are listed in Table S5.6. Orange diamonds represent sample **6** on SiNx chips with 100 nm aperture diameters monitored in 1.0 M NaCl + 10 mM HEPES. Black dots represent samples on SiNx chips with 500 nm aperture diameters monitored in 1.0 M NaCl + 10 mM HEPES. Blue dots represent samples on SiNx chips with 500 nm aperture diameters monitored in 3.6 M NaCl + 10 mM HEPES. Red crosses represent sample **55** fabricated during pore nucleation without any pore enlargement on SiNx chips with 500 nm aperture diameters monitored in 3.6 M NaCl + 10 mM HEPES. Green triangles represent samples on SiNx chips with 500 nm aperture diameters monitored in 1.0 M NaCl + 10 mM HEPES + 10 µM SDS.

Nanopore stability upon flushing

After the processes of nanopores nucleation and enlargement, usually the chambers are replaced with a fresh electrolyte solution. When this flushing operation is performed, it is important to verify that during flushing, the conductance remains unchanged. To investigate whether flushing could influence the pore characteristics, the pore conductance was monitored before and after flushing in 1.0 M NaCl (Figure 5.8A and B). The results are listed in Table S5.6. For graphene nanopore sample **6** on a SiNx chip with 100 nm aperture diameter, a conductance of 67 nS was measured in 1.0 M NaCl after a waiting time of 10 min after fabrication. The fluidic cell was

then repeatedly flushed with fresh 1.0 M NaCl solution, and the pore conductance was measured after each flush, which ranged from 63 to 67 nS in 1.0 M NaCl. The pore conductance seemed exceptionally stable over 9 flushes in 1.0 M NaCl, with changes of <5% upon flushing (orange diamonds in Figure 5.8A). In SiNx chips with 500 nm aperture diameter, a reduction in conductance of >10% could be occasionally observed after flushing. These reductions were observed both for samples fabricated without the presence of SDS (black dots in Figure 5.8) and samples fabricated in the presence of SDS (green triangles in Figure 5.8). Since changes of <10% in conductance over time seemed reasonable over the duration of the experiment, changes of >10% could be explained by clogging of the pores as a result of flushing. The reduced conductance could be reverted to the original conductance after additional flushes, indicating that the pore clogging was reversible. Over 15 flushes, 7 flushes resulted in decreases in conductance of >10%, which translates to a 47% chance of clogging when flushing with 1.0 M NaCl in 500 nm chips. The chance of clogging could be sample-dependent and related to the individual pore sizes, where samples with smaller pores are more prone to clogging.

To investigate whether SDS could influence the conductance of graphene nanopores fabricated by controlled breakdown, the conductance was measured before and after flushing with 1.0 M NaCl solutions with and without SDS (Figure S5.7). For graphene nanopore sample **6** on a SiNx chips with 100 nm aperture diameter, a conductance of 65 nS was measured in 1.0 M NaCl after the final flush with 1.0 M NaCl (orange diamonds in Figure 5.8A). Then, after flushing this sample with 1.0 M NaCl + 10 μM SDS, a similar pore conductance of 68 nS was measured (orange diamond in Figure 5.8C). After flushing again with fresh 1.0 M NaCl solution without SDS, a similar conductance of 67 nS was recorded (orange diamond in Figure 5.8D). In SiNx chips with 500 nm aperture diameter, the conductance also remained similar (changes <20%) before and after flushing with SDS containing solution, both for samples fabricated without the presence of SDS (black dots in Figure 5.8C) and in the presence of SDS (green triangles in Figure 5.8C). *Vice versa*, upon flushing with 1.0 M NaCl + 10 μM SDS, no clear change in conductance was observed other than several clogging events (reduction in pore conductance of >20%) (Figure 5.8D). These results suggest that the presence of SDS does not influence the pore conductance significantly. Interestingly, the chance for clogging in 500 nm chips seems slightly reduced when SDS is present before or after flushing (5 out of 18 flushes, 28%) compared to flushing when SDS is absent (47%). These results suggest that SDS can have a beneficial effect on preventing pore clogging upon flushing.

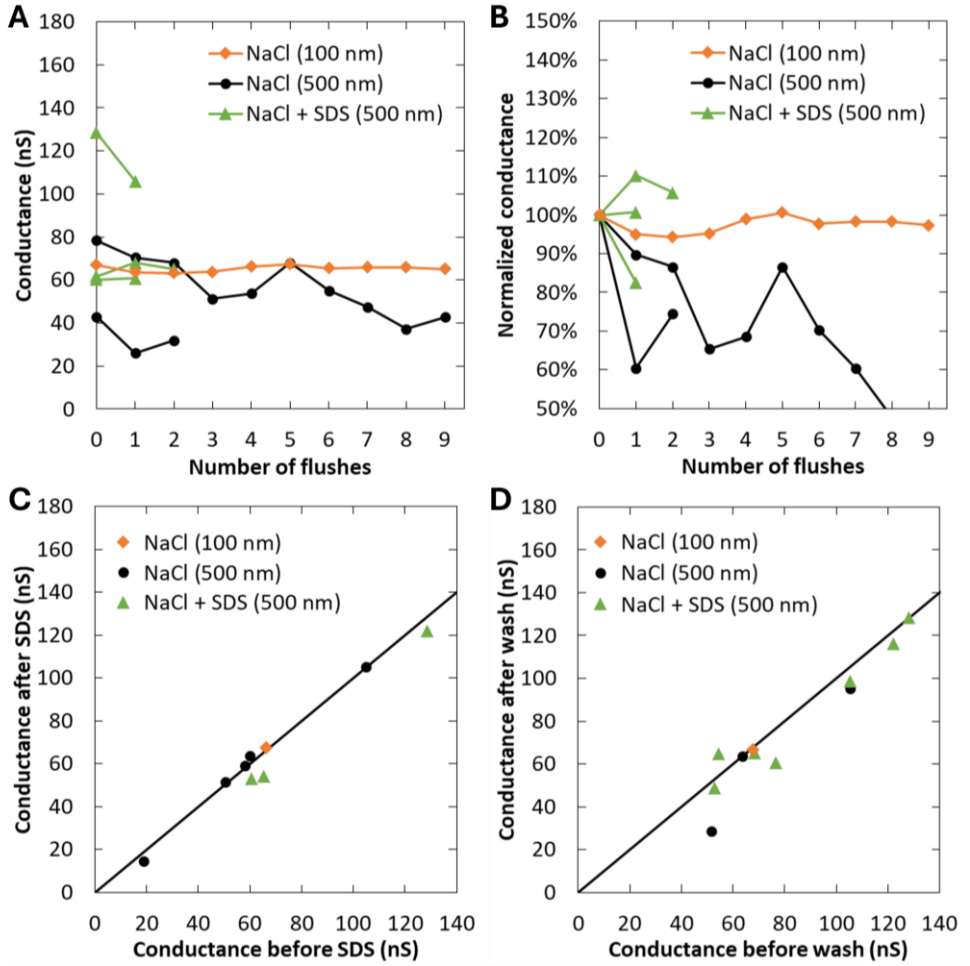

Figure 5.8 Graphene nanopore stability after flushing with NaCl solutions with and without SDS. (A) The conductance after each flush with 1.0 M NaCl + 10 mM HEPES. (B) The normalized conductance after each flush with 1.0 M NaCl + 10 mM HEPES. (C) Conductance (in nS) of graphene nanopores measured first in 1.0 M NaCl + 10 mM HEPES (x-axis) and then measured in 1.0 M NaCl + 10 mM HEPES + 10 μM SDS (y-axis). The results are listed in Table S5.6. (D) Conductance (in nS) of graphene nanopores measured first in 1.0 M NaCl + 10 mM HEPES + 10 μM SDS (x-axis) and then measured in 1.0 M NaCl + 10 mM HEPES (y-axis). The results are listed in Table S5.6. Orange diamonds represent sample **6** fabricated on SiNx chips with 100 nm aperture diameter without the presence of SDS. Black dots represent samples fabricated on SiNx chips with 500 nm aperture diameter without the presence of SDS. Green triangles represent samples fabricated on SiNx chips with 500 nm aperture diameter in the presence of SDS.

5.2.5 Noise of graphene nanopores fabricated by CBD

Noise in ionic current readings is an important aspect of biomolecule recognition in nanopores, since low noise is necessary to obtain sufficient signal-to-noise ratio.[66] Noise in solid-state nanopores can be quantified as the sum of four different components, with each component dominating a certain frequency (*f*) range from low to high:[67] flicker noise (1/*f* noise),[68,69,16,70] white noise (shot and thermal noise),[70,71] dielectric noise[71] and capacitive noise (Figure 5.9A).[72] Generally, the 1/*f* noise is particularly large in graphene nanopores compared to biological nanopores and thicker solid-state nanopores.[66] This large 1/*f* noise in graphene is attributed to a combination of many origins,[69,73,70,74,75] including poor wetting[76] and mechanical fluctuations.[77,78] Wetting can be increased by adding hydrophilic coatings to the membrane,[13,79,80] or by minimizing contamination by piranha treatment.[81] Mechanical fluctuations can be decreased by reducing the free-standing area,[73,82,83] or by increasing the thickness of the 2D material.[77] These aspects are actively explored to increase the signal-to-noise ratio for eventual use of graphene nanopores in sensing applications.[70,66,67] Here, we investigated the noise in graphene nanopores fabricated by controlled breakdown.

To quantify the 1/*f* noise, the current (*I*) was measured at a fixed bias voltage of -100 mV in 1.0 M NaCl + 10 mM HEPES at a 1 kHz bandwidth (low-pass Bessel filter) and measured over 200 ms (Figure 5.9B). The filter was applied to simplify the ionic current readout and was assumed not to interfere with the 1/*f* noise in the low-frequency regime. By applying Fourier transformation to the *I*-t trace, the frequency components of the noise were extracted to afford the current power spectral density (S_I), which describes the noise distribution in the low-frequency regime ($f < 1000$ Hz) (Figure 5.9C). Since S_I values increase with increasing values of *I*, the S_I values were normalized to allow comparison between different conditions according to equation (3):

$$\frac{S_I}{I^2} = \frac{A}{f}, \quad (3)$$

where *A* is a dimensionless parameter representing the 1/*f* noise amplitude. The value for *A* was obtained as the intersect at 1 Hz after linear regression in double logarithmic space over the low-frequency regime (Figure 5.9D, see methods section) and the values of *A* for each sample are listed in Table S5.8.

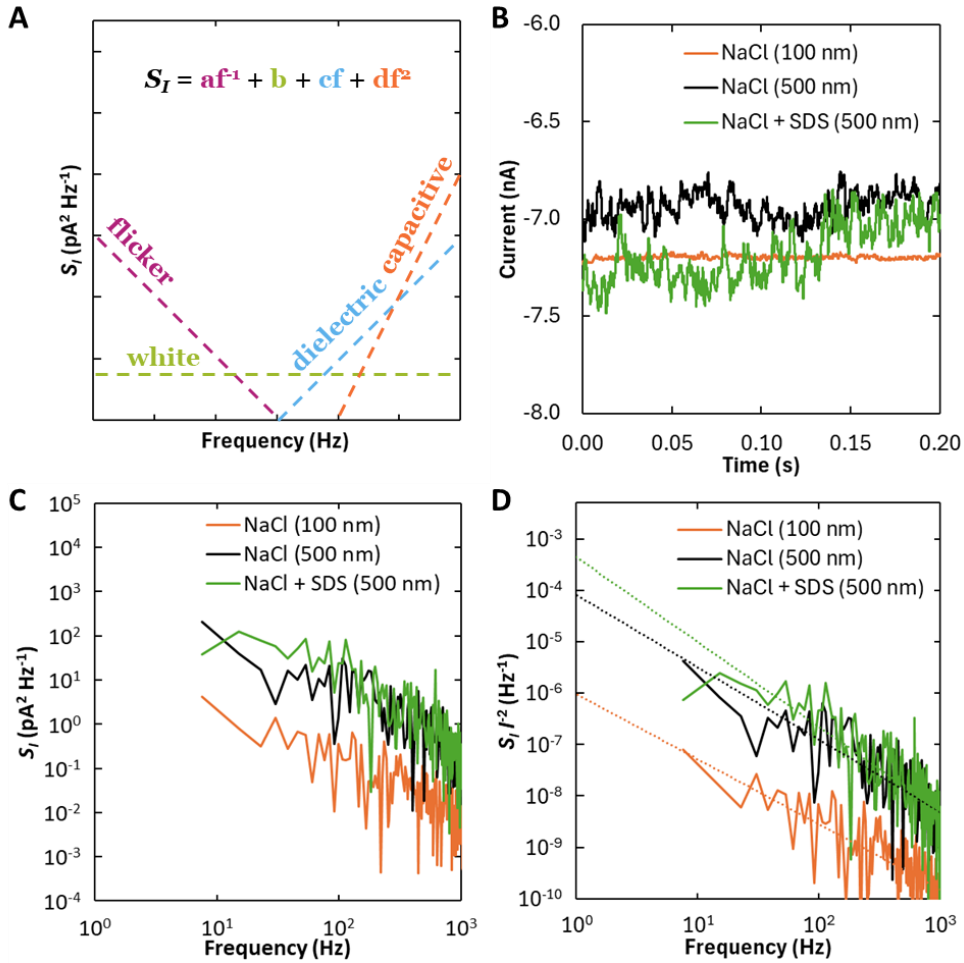

Figure 5.9 Noise characterization in graphene nanopores fabricated by controlled breakdown. (A) Illustration of the current power spectral density (S_I, in pA^2 Hz^{-1}) plotted against frequency (in Hz), which describes the frequency dependence of the flicker noise (purple), white noise (green), dielectric noise (blue) and capacitive noise (orange). (B) The current (in nA) plotted against time (in s) at a fixed bias voltage of -100 mV for graphene nanopores in 1.0 M NaCl + 10 mM HEPES. (C) The S_I values (in pA^2 Hz^{-1}) plotted against frequency (in Hz) extracted from the current-time traces in panel B. (D) The normalized 1/*f* noise ($S_I I^{-2}$, in pA^2 Hz^{-1}) plotted against frequency (in Hz) extracted from panels B and C. The value for *A* was obtained as the intercept at $f = 1$ Hz by linear regression in double logarithmic space (see methods section). Orange traces represent sample **6** fabricated on a SiNx chip with 100 nm aperture diameter without the presence of SDS. Black traces represent sample **44** fabricated on a SiNx chip with 500 nm aperture diameter without the presence of SDS. Green traces represent sample **52** fabricated on a SiNx chip with 500 nm aperture diameter in the presence of SDS.

Influence of fabrication conditions on 1/*f* noise

To investigate the influence of fabrication conditions on the noise, the samples were divided into three categories, with one example of each category shown in Figure 5.9B–D: nanopores fabricated on SiNx chips with 100 nm aperture diameter without the presence of SDS (orange trace), nanopores fabricated on SiNx chips with 500 nm aperture diameter without the presence of SDS (black trace) and nanopores fabricated on SiNx chips with 500 nm aperture diameter in the presence of SDS (green trace). In general, the dominance of 1/*f* noise was observed for all samples (Figure 5.9C), which is characteristic for graphene nanopores.[77] The current power spectral density (S_I) did not seem dependent on time after fabrication, nor on whether SDS was added to the electrolyte solution, as changing either of these parameters did not result in significant changes in the power spectra (Figure S5.8). The 1/*f* noise amplitude (A) was extracted (see methods section) and plotted against the apparent pore diameter and pore resistance (Figure 5.9D). For graphene nanopores fabricated on SiNx chips with 100 nm aperture diameter, the 1/*f* noise amplitude, A_{100nm} (± SE), was $1.5 \pm 1.6 \times 10^{-5}$ (N = 7) (Table S5.8). For nanopores fabricated on SiNx chips with 500 nm aperture diameter, A_{500nm} was $6.2 \pm 3.0 \times 10^{-5}$ (N = 24) (Table S5.8). The higher value of A_{500nm} compared to A_{100nm} can be explained by increased mechanical fluctuations in larger free-standing areas.[73,82,83] For nanopores fabricated on SiNx chips with 500 nm aperture diameter in the presence of SDS, A_{SDS} was $14 \pm 15 \times 10^{-5}$ (N = 7) (Table S5.8). Because of the large variance in data, it was not clear whether fabrication in SDS could influence the 1/*f* noise (p = 0.35). In general, the values for A were an order of magnitude higher than for graphene nanopores fabricated by TEM drilling[77] and the ultra-short, high-voltage pulse CBD method,[39] suggesting that differences in fabrication technique can play a role in the resulting 1/*f* noise in graphene nanopores.

Influence of pore characteristics on 1/*f* noise

To investigate the influence of the pore characteristics on the noise, the values for A were plotted against the apparent pore size, *e.g.* the diameter of a hypothetical single pore converted from the measured conductance according to Equation (1), and pore resistance (Figure 5.10). Again, the samples were divided into three categories: nanopores fabricated on SiNx chips with 100 nm aperture diameter without the presence of SDS (orange diamonds) (N = 7), nanopores fabricated on SiNx chips with 500 nm aperture diameter without the presence of SDS (black dots) (N = 24) and nanopores fabricated on SiNx chips with 500 nm aperture diameter in the presence of SDS (green triangles) (N = 7). A large variation in the extracted values of A could be observed for each category, and no significant differences could be

observed between the different categories at these sample sizes. Still, a linear correlation can be observed in the logarithmic space between A and the apparent pore diameter (d) and pore resistance (R) across all samples. These correlations follow the relationships of $A \sim d^{-\gamma_1}$ and $A \sim R^{\gamma_2}$, where the exponents (± SE) were extracted by linear regression in logarithmic space with $\gamma_1 = 1.4 \pm 0.8$ and $\gamma_2 = 1.3 \pm 0.8$ (see methods section). These values for γ_1 and γ_2, as well as the large variance in data, are similar to the values found for graphene nanopores fabricated by TEM drilling,[77] suggesting that the underlying mechanisms for noise dependencies on pore size and resistance are similar across different fabrication techniques.

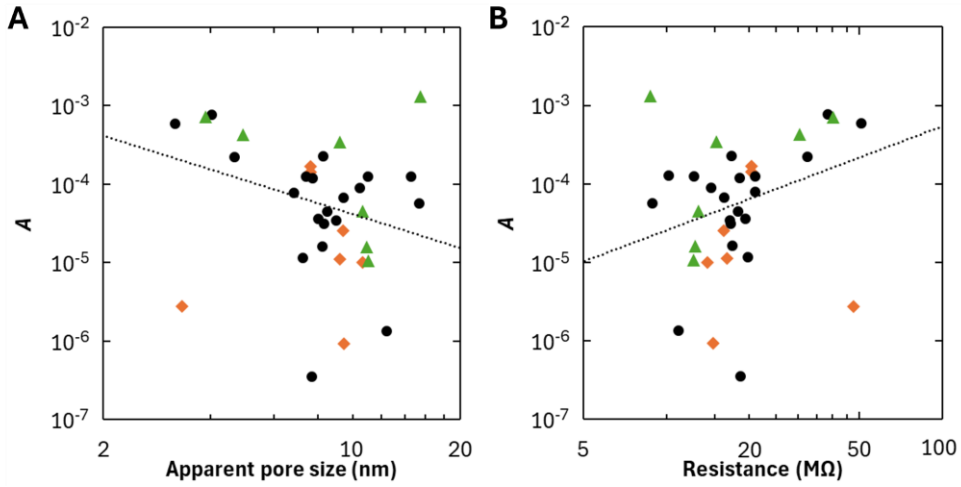

Figure 5.10 Influence of apparent pore size and pore resistance on 1/*f* noise in graphene nanopores fabricated by controlled breakdown. (A) The value for A plotted against the apparent pore size (d, in nm), which was calculated according to Equation (1) assuming that only a single pore in the graphene membrane was created by controlled breakdown. (B) The value for A plotted against the pore resistance (R, in MΩ). Linear regression in double logarithmic space afforded the trendlines $A \sim d^{-\gamma_1}$ and $A \sim R^{\gamma_2}$ in panels A and B, respectively. Black dots represent samples fabricated on SiNx chips with 100 nm aperture diameters without the presence of SDS and measured in 1.0 M NaCl + 10 mM HEPES. Orange diamonds represent samples fabricated on SiNx chips with 500 nm aperture diameters without the presence of SDS and measured in 1.0 M NaCl + 10 mM HEPES. Green triangles represent samples fabricated on SiNx chips with 500 nm aperture diameters in the presence of SDS and measured in 1.0 M NaCl + 10 mM HEPES + 10 µM SDS. The results are listed in Table S5.7.

Influence of wettability and pore size on 1/*f* noise

Finally, to investigate the influence of wettability on the noise, values for A were extracted before and after coating with PPEG (Table S5.5). In sample **19**, 1/*f* noise decreased by an order of magnitude after coating with PPEG, from $A_{bare} = 2.6 \pm 1.9 \times 10^{-5}$ for bare graphene (black trace) to $A_{PPEG} = 2.9 \pm 2.0 \times 10^{-6}$ after PPEG coating (red trace) (Figure 5.11A). This was also the only sample for which a decrease in 1/*f* noise was observed after PPEG coating (Figure 5.6B). A decrease in 1/*f* noise is expected for graphene nanopores coated with a hydrophilic coating due to increased wettability,[13,79,80] which can be facilitated by the polyethylene glycol moieties of the PPEG coating. In contrast, an increase in 1/*f* noise was observed for most samples after coating with PPEG (Figure 5.11B). For samples measured without the presence of SDS (black dots), a relatively large increase in 1/*f* noise was found after PPEG coating (red squares). We hypothesize that the increase in 1/*f* noise after coating is due to fluctuating obstruction of the pores by the adsorbed coating molecules. Because the magnitude of pore obstruction is relatively smaller in larger pores, the resulting change in noise could vary from sample to sample depending on the pore size. Finally, for samples measured in the presence of SDS (green triangles), the change in 1/*f* noise was sometimes negligible after coating (purple diamonds). This negligible change could be explained because of SDS having similar effects as the PPEG coating,[54] both in terms of wettability and pore obstruction. Therefore, changing the coating from SDS to PPEG may not influence the 1/*f* noise significantly.

To investigate how the 1/*f* noise scaled with pore size, A before and after PPEG coating was plotted against individual pore size (d), *e.g.* diameter per pore (assuming evenly distributed pore sizes) (Figure 5.11B, see methods section). It is important to note that the assumption was drawn that sample **19** contains a single pore, where the negligible decrease in conductance from 58 nS before coating to 55 nS after coating with PPEG in Figure 5.6B was masked by damage to an existing single pore from flushing. Overall, the 1/*f* noise seemed to increase with decreasing individual pore size. Before PPEG coating, a linear correlation was observed in semi-logarithmic space between A and individual pore size across all samples without any coating (black trace) (N = 3). A steeper linear correlation was observed after PPEG coating (red trace). While the exact reason for these correlations is not clear, these correlations follow the relationships of $A_{bare} \sim e^{-\gamma_3 d}$ and $A_{PPEG} \sim e^{-\gamma_4 d}$, where the coefficients (± SE) were extracted by linear regression in semi-logarithmic space with $\gamma_3 = 0.13 \pm 0.01$ and $\gamma_4 = 0.64 \pm 0.08$. The point at which the decreasing effect of PPEG coating on the 1/*f* noise (due to increased wettability) is cancelled out by

the increasing effect on the 1/*f* noise (due to fluctuating obstruction) can be found at the x-coordinate of intersection ($X \pm$ SE), which is 7.6 ± 1.7 nm. This means that for a membrane consisting of 6 – 9 nm diameter pores, the 1/*f* noise before and after hydrophilic coating is expected to exhibit similar values. For membranes with pores larger than 9 nm, a hydrophilic coating reduces the 1/*f* noise. For membranes with pores smaller than 6 nm, the coating increases the 1/*f* noise. These results suggest that monitoring the 1/*f* noise using PPEG coating may be a useful indicator for distinguishing individual pore size, and indirectly also multiporosity if the pores are in the relevant size range, in graphene membranes. It is important to stress again that sample **19** was assumed to contain a single pore despite negligible decrease after PPEG coating, though similar trends would still be observed if this sample was omitted (Figure S5.9).

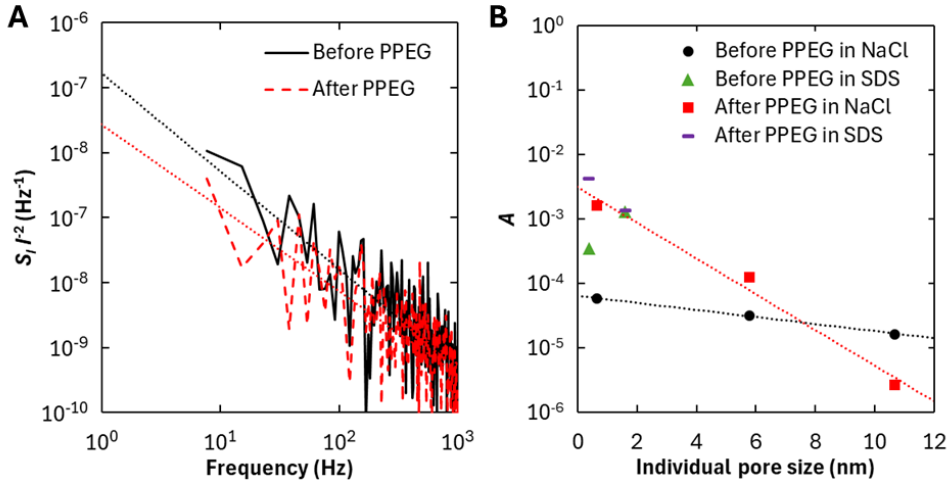

Figure 5.11 Influence of PPEG coating on 1/*f* noise in individual graphene nanopores on SiNx chips with 500 nm aperture diameter fabricated by controlled breakdown. (A) The normalized 1/*f* noise ($S_I I^{-2}$, in pA^2 Hz^{-1}) plotted against frequency (in Hz) for sample **19** before (black trace) and after PPEG coating (red dashed trace) in 1.0 M NaCl + 10 mM HEPES. The value for *A* was obtained as the intercept at f = 1 Hz by linear regression in double logarithmic space (see methods section). (B) The values for *A* plotted against the individual pore size (in nm) before and after PPEG coating. Black dots represent samples measured in 1.0 M NaCl + 10 mM HEPES before PPEG coating. Green triangles represent samples measured in 1.0 M NaCl + 10 mM HEPES + 10 µM SDS before PPEG coating. Red squares represent samples measured in 1.0 M NaCl + 10 mM HEPES after PPEG coating. Purple dashes represent samples measured in 1.0 M NaCl + 10 mM HEPES + 10 µM SDS after PPEG coating. The trendlines were obtained from linear regression in semi-logarithmic space (see methods section). The results are listed in Table S5.5.

5.3 Conclusions

In summary, we have developed a procedure to reliably fabricate and characterize single and multiple graphene nanopores in NaCl using automated controlled breakdown. In terms of software control, the nucleation current threshold, enlargement pulse duration, and quick measure waiting time were optimized to offer a reproducible and scalable process for graphene nanopore fabrication. The nucleation voltage, nucleated pore size, and enlargement efficiency seemed decreased for samples on SiNx chips with 500 nm aperture diameter compared to 100 nm aperture diameter, suggesting that the controlled breakdown process is dependent on the free-standing graphene area. The number of pores in each sample seemed to vary from one to 23 according to PPEG coating experiments despite following a protocol similar to one that could reliably produce single nanopores in SiNx membranes,[41] suggesting that the type of material is a critical parameter in single nanopore fabrication by CBD.

After the process of pore nucleation and pore enlargement, the conductance of graphene nanopores fabricated on SiNx chips with 500 nm aperture diameter generally decreased by up to 38% over 2 h in 1.0 M and 3.6 M NaCl solutions, suggesting that graphene nanopores fabricated by CBD are not stable in NaCl solutions. In contrast, a sample fabricated after pore nucleation without pore enlargement showed an increase in conductance from 171 nS to 197 nS in 3.6 M NaCl over 20 min after fabrication, suggesting that the nanopore fabrication process may affect the pore stability. The variation in pore stability may be related to the individual pore sizes of graphene nanopores per sample, where samples with smaller pores are more prone to clogging.

Moreover, small amounts of SDS added to the electrolyte during and after controlled breakdown were demonstrated to influence the controlled breakdown process and nanopore stability, respectively. The presence of SDS during the fabrication process did not significantly influence the nucleation voltage, which suggests that the barrier for pore nucleation in graphene is not dependent on the wettability of the graphene. In contrast, the presence of SDS accelerated pore enlargement, presumably by increasing the wettability of the graphene. The presence of SDS after fabrication seemed to increase both long-term and flushing stability, possibly by solubilization of residual hydrocarbons and prevention of hydrocarbon adsorption to the graphene.

Finally, we have characterized the 1/*f* noise in graphene nanopores fabricated by controlled breakdown. The 1/*f* noise amplitude in these pores was an order of

magnitude higher than in graphene nanopores fabricated by TEM drilling, suggesting that the fabrication technique is an important factor for the 1/*f* noise. Additionally, both types of graphene nanopores exhibited similar correlations with apparent pore size and resistance, suggesting that these relationships are intrinsic to graphene nanopores. Lastly, the presence of PPEG coating seemed to either increase or reduce the 1/*f* noise depending on the graphene nanopore diameter, suggesting that hydrophilic surface coatings have an effect on both wettability and fluctuations in pore obstruction. Therefore, monitoring the effect on the 1/*f* noise after PPEG coating can give additional insight into the individual pore size and multiporosity of the membrane, where an increase or a decrease in 1/*f* noise after coating indicates individual pore sizes of <6 nm or >9 nm, respectively.

5.4 Future prospects

We anticipate that single graphene nanopores can be reliably fabricated after additional optimization in software control and fabrication conditions. First, it is necessary to investigate whether the formation of multiple pores occurs during pore nucleation step or during the pore enlargement step, which would require further studies dedicated to investigating correlations between multiporosity versus nucleation parameters and enlargement parameters. If the pore is formed during the pore nucleation step, it may be useful to decrease the current threshold, voltage ramp speed, electrolyte concentration or pH of the buffer. If the pore is formed during the enlargement step, it may be useful to change the pulse duration, direction of the applied potential (*e.g.* only positive instead of alternating current), electrolyte composition and other buffer properties. Alternatively, it could be useful to perform both pore nucleation and pore enlargement using ultrashort pulse durations (250 ns) of higher voltages (5 – 7 V) similar to the ones used by Kuan et al.[39] Notably, the increased voltage requirement during fabrication, enhanced stability and reduced 1/*f* noise amplitude in SiNx chips with 100 nm aperture diameter suggest that the nature of these pores is different from pores fabricated in SiNx chips with 500 nm aperture diameter, and warrants further investigation into multiporosity in SiNx chips with 100 nm aperture diameter.

Second, voltage mediated delamination (VMD) complicates the reproducibility of nanopore fabrication. VMD may be less frequent by enhancing the adhesion of graphene to the substrate. Even though we use a pyrene adhesion layer, this may not be sufficient to fully immobilize the graphene onto the substrate. The pyrene adhesion layer increased the roughness of the substrate, which could compromise the immobilization of the graphene onto the substrate.[50] Therefore, a better

alternative could be using an adhesion layer that retains the homogeneity of the SiNx substrate, such as fluoroalkylsilane functionalization.[84,85] Notably, even though graphene is generally considered hydrophobic, a hydrophilic coating could improve adhesion of wet-transferred graphene as a result of capillary forces.[85]

Finally, characterization of small (~10 nm) graphene nanopores without relying on electron microscopy can drastically increase the throughput and reduce the cost of quality control for fabricated graphene nanopores. The PPEG coating experiments indicated that, after coating, the $1/f$ noise is decreased in samples with >9 nm nanopores but increased in samples with <6 nm nanopores. These experiments can be performed cost and time efficiently, and do not expose the graphene to potential electron beam damage or hydrocarbon contamination during TEM. However, PPEG coating also cannot be completely removed by simple solvation due to its strong adhesion to graphene. Therefore, for these samples to remain usable after PPEG coating experiments, methods for efficient coating removal should be further investigated, for example using thermal annealing treatment, plasma treatment, and light treatment, among many others.[58]

5.5 Materials and Methods

SiNx chips with 100 nm apertures (NXPR5002Y-C0.10-AO-HR) or 500 nm apertures (NXPR5002Y-C0.50-AO-HR) were obtained from Norcada. These chips consisted of a 20 nm thick SiNx membranes of 20 × 20 μm and a 60 nm SiO_2 under layer in a 200 μm thick square silicon frame of 5 × 5 mm. Single-crystal CVD graphene on copper was obtained from Beijing Graphene Institute. Ultrapure water, with a resistivity of 18.2 MΩ·cm, was obtained from a Millipore Milli-Q gradient A10 system. Gases were supplied by Linde Gas (5.0). All chemicals, including sodium chloride (NaCl), 4-(2-hydroxyethyl)-1-piperazineethanesulfonic acid (HEPES), sodium dodecyl sulfate (SDS), acetone, isopropyl alcohol (IPA), ethanol (EtOH), methanol (MeOH), ammonium persulfate (APS), N-dimethylformamide (DMF), 1-[bis(dimethylamino)methylene]-1H-1,2,3-triazolo[4,5-b]pyridinium 3-oxid hexafluorophosphate (HATU), 3-aminopropyl-triethoxysilane (APTES), 1-pyrenebutyric acid (PBA), and triethylamine (NEt_3), were purchased from Sigma–Aldrich, and used as received without further purification. Poly(methyl methacrylate) (PMMA) with a concentration of 6% in anisole (AR-P 662.06) was purchased from Allresist GmbH. Conductivity standard solutions (84 μS cm^{-1} and 12880 μS cm^{-1}) and pH standard solutions (pH 4.01, pH 7.01 and pH 10.01) were purchased from Hanna Instruments.

5.5.1 Graphene sample preparation

Pyrene functionalization of the SiNx chip was performed according to a protocol adapted from Geest et al.[86] SiNx chip was first cleaned by applying oxygen plasma at 200 W (100%), 0.20 mbar for 120 s using a capacitively coupled plasma (CCP) system from Diener electronics. Within 2 h after plasma treatment, the chips were submerged in a solution of APTES (0.34 mL, 1.5 mmol) and glacial acetic acid (2.0 µL, 35 µmol) in EtOH 96% (20 mL). After 10 min, the chips were rinsed using EtOH and dried using a N_2 gun. Then, the chips were submerged in a solution of pyrene butyric acid (129 mg, 0.45 mmol) and HATU (253 mg, 0.67 mmol) in DMF (30 mL). After adding 10 drops of Et_3N, the chips were left for 3 d. Then, the chips were rinsed thoroughly using acetone and EtOH, and dried using a N_2 gun. Contact angle experiments were performed by vertically placing a 2 µL droplet of ultrapure water on the chip at room temperature using a micropipette, then recording a snapshot within 5 s to prevent evaporation effects. Snapshots were collected on a Ramé-Hart 250 goniometer (Netcong, NJ) and processed using DROPimage advanced v2.8 software.

PMMA-assisted wet transfer of graphene was performed according to the protocol of Kang et al.[50] Top-side graphene was spin-coated with PMMA in anisole (~70 µl cm^{-2}) using a POLOS SPIN 150i table top spin coater (4000 rpm, 60 s) and then put on a hot plate at 80 °C to allow anisole to evaporate. With the PMMA side down, back-side graphene was then removed by applying oxygen plasma at 100 W (50%), 0.20 mbar for 120 s using a CCP system from Diener electronics. Copper was etched by floating the copper foil with the graphene/PMMA side up on a 0.5 M aqueous ammonium persulfate (APS) solution (200 mL) until the copper was completely dissolved. The graphene/PMMA film was then transferred into three ultrapure water baths (2 × 200 mL, 1 × 600 mL) to remove excess APS. The graphene/PMMA was transferred onto the pyrene-functionalized SiNx chip by bottom fishing and allowed to dry over air overnight. The sample was annealed on a hot plate at 50℃, 100℃ and then 120℃ for 10 min, 5 min, and 20 min, respectively. The PMMA was removed by submerging in three acetone baths (50 mL) for 10 min, 10 min, and 60 min, and then rinsing using acetone and EtOH before drying using a N_2 gun. Optical microscopy images were obtained using Leica DM 2700 m Brightfield microscope equipped with a Leica MC 120 HD camera. Raman experiments were performed by placing a Si/SiO_2 wafer underneath the graphene-transferred SiNx chip, then recording the spectra using a 100× objective lens and 532 nm laser (~2 mW). Raman spectra were collected on a WITEC alpha500 R Confocal Raman Imaging instrument and processed using WITEC GmbH software and Microsoft® Excel®.

5.5.2 Buffer preparation

Buffer preparation was performed according to the protocols described by Waugh et al.[41] Aqueous NaCl solutions were obtained by dissolving NaCl (29 g, 0.50 mol, 1.0 M, or 105 g, 1.80 mol, 3.6 M) and (4-(2-hydroxyethyl)-1-piperazineethanesulfonic acid) (HEPES) (1.19 g, 5.00 mmol, 10 mM) in ultrapure water (500 mL). The obtained NaCl solutions (pH 5.5 – 6.0) were then titrated using 1.0 M NaOH while stirring to obtain the final NaCl solutions of 1.0 M NaCl + 10 mM HEPES (7.76 S m^{-1}) and 3.6 M NaCl + 10 mM HEPES (18.89 S m^{-1}) with pH 8.0. For the preparation of NaCl + 10 µM SDS solutions, a methanolic stock solution of sodium dodecyl sulfate (SDS) (29 mg, 0.1 mmol, 1.0 mM) was prepared in MeOH (100 mL). To obtain the aqueous NaCl + 10 µM SDS solutions, an aliquot of the SDS stock solution (1.0 mL, 1.0 µmol, 1.0 mM in MeOH) was allowed to evaporate and then redissolved in 1.0 M NaCl + 10 mM HEPES (100 mL) or 3.6 M NaCl + 10 mM HEPES (100 mL) to obtain 1.0 M NaCl + 10 mM HEPES + 10 µM SDS (7.68 S m^{-1}) and 3.6 M NaCl + 10 mM HEPES + 10 µM SDS (18.89 S m^{-1}), respectively. The conductivity of the buffer solutions was measured at room temperature using an Edge EC 240V (HI2003-02) conductometer from Hanna Instruments, which was calibrated using conductivity standards of 84 µS cm^{-1} and 12880 µS cm^{-1}. The pH was measured using at room temperature an Edge (HI2020-02) pH meter from Hanna Instruments, which was calibrated using pH standards of 4.01, 7.01 and 10.01. All solutions were filtered through a CHROMAFIL Xtra disposable filter PET-20/13 (0.20 µm pore diameter, 13 mm membrane diameter) before use in the fluidic cell.

5.5.3 Graphene nanopore fabrication by controlled breakdown

Electrode preparation, chip mounting, and membrane wetting were performed according to the protocols described by Waugh et al.[41] The graphene samples on SiNx chips were mounted between two silicone gaskets in a 5 × 5 mm fluidic cell. After mounting the chips, the membranes were wetted by carefully flushing isopropanol (1 × 100 µL) through each half-cell. Care was taken to avoid introduction of air into the flow cell, and any excess solution in the overflow wells was removed after each flush by pipetting carefully to avoid air from entering the flow cell. Note that rapid flushing may prevent proper wetting of the membrane. Then, each half-cell was carefully flushed with the respective buffer solution for nucleation (6 × 100 µL). The Ag/AgCl electrodes were held and aligned by anti-evaporation caps. Electrodes that showed signs of degradation (discoloration) were sanded and replated by immersing in Clorox bleach for at least 30 min. Note that the portion protruding out of the evaporation cap should be unplated, and therefore

sanded if necessary, to avoid damaging the instrument. After successful nucleation, if a change of buffer solution was necessary, each half-cell was carefully flushed with the respective buffer solution for enlargement (6 × 100 µL). After finishing the experiments, the chips were dismounted, rinsed with H_2O and EtOH, dried using a N_2 gun, and stored under vacuum.

Controlled breakdown was performed using the Northern Nanopore Instruments (NNi) Spark-E2 system and the dedicated Nanopore Fabrication software as described by Waugh et al.[41] The software parameters for nucleation and enlargement are listed in Table S5.9. Data analysis was performed in Microsoft® Excel®. The standard deviations of the nucleation voltage, nucleated pore diameter, enlargement voltage and enlargement efficiency were calculated *via* the STDEV function in Microsoft® Excel®. The standard errors of the nucleation voltage, nucleated pore diameter, enlargement voltage and enlargement efficiency were calculated according to equation (4). The p-values were calculated according to Student's *t*-test (two-tailed, heteroscedastic) *via* the T.TEST function in Microsoft® Excel®.

$$(4) \quad SE = \frac{\sigma}{\sqrt{N}}$$

5.5.4 PPEG coating experiments

PPEG coating was performed according to the protocol described by Kuan et al.[39] Both half-cells of the fluidic cell was flushed water (3 × 100 µL), then MeOH (3 × 100 µL), and then filled with 1-aminopyrene in MeOH (10 mg mL^{-1}). After 10 min, the fluidic cell was flushed with MeOH (3 × 100 µL) and then filled with methyl-PEG_4-NHS ester in MeOH (10 mg mL^{-1}). After 10 min, the fluidic cell was rinsed with MeOH (3 × 100 µL), then water (3 × 100 µL), and then filled with measuring buffer. Note that repeated PPEG coating experiments in the fluidic cell resulted in discoloration of the fluidic cell, therefore it is recommended to perform the coating experiments after dismounting the chips in a separate container. The number of pores were calculated by non-linear regression using Microsoft® Excel® Solver according to Equation (2). Assuming that the experimental conductance was evenly divided over the number of pores, the individual pore size was calculated according to equation (1).

5.5.5 Conductance and noise analysis

The current (*I*) was recorded at room temperature in a Faraday cage on a vibration isolation table using an Axopatch 200B amplifier (Molecular devices) coupled with a Digitizer 1550 (Molecular Devices). Ionic currents were detected at a 1 kHz

bandwidth (low-pass Bessel filter) and digitized at 10 kHz. All potentials were referenced to the saturated Ag/AgCl electrode in the female, smaller half-cell. Pore conductance values were obtained by monitoring the current between -100 mV and 100 mV with steps of 10 mV for 1 s each. After allowing the capacitive transient to decay for 600 ms, the average current between 600 and 800 ms was plotted against the applied potential to obtain the current-voltage (I-V) curves. The slope of the I-V curve was obtained by linear regression using Clampfit software to afford the conductance values.

Current traces for noise analysis were obtained by monitoring the current at a fixed voltage bias of -100 mV. After allowing the capacitive transient to decay for 600 ms, the steady-state current was monitored over the following 200 ms. The S_I was then extracted for the frequencies f between 7 – 250000 Hz using Clampfit. Equation (3) was converted to logarithmic space according to Equation (5), which takes the form of a linear function as described by Equation (6), where $y = \log\left(\frac{S_I}{I^2}\right)$, $a = -1$, $x = \log(f)$, and $b = \log(A)$. Taking the logarithm of $S_I I^{-2}$ values and the logarithm of f values between 1 – 1000 Hz, linear regression was performed using the LINEST function in Microsoft® Excel® to afford the value for b and its standard error (SE_b). The value for A was calculated according to Equation (7). The standard error of A (SE_A) was obtained through error propagation of SE_b according to Equation (8). The geometric mean (A_{avg}) was calculated by taking the arithmetic mean of the log-transformed data and retransforming to the original scale.

The values and standard errors (SE) of the coefficients γ_1 and γ_2 were obtained from linear regression in double logarithmic space using similar methods as above, including the LINEST function in Microsoft® Excel®. The coefficients for the exponential relationships in Figure 5.11B were obtained from the linear correlations observed on the semi-logarithmic plots of A over individual pore size (d). The data was linearized by transforming the exponential equation (9) into equation (10) using the natural logarithm. The coefficients (slopes a_1, a_2, and logarithmic intercepts $\ln(b_1)$, $\ln(b_2)$) of the two functions and their standard errors were determined using the LINEST function in Microsoft® Excel®. These coefficients were used for the calculation of the x-coordinates (in geometric scale) and y-coordinates (in logarithmic scale) of intersection (X and $\ln(Y)$, respectively) according to Equations (11) and (12), respectively. Their standard errors SE_X and $SE_{Y,ln}$ were propagated according to Equations (13) and (14), respectively. The values for Y and SE_Y were calculated by converting logarithmic scale back to original scale according to Equations (15) and (16), respectively.

(5) $\log\left(\frac{S_I}{I^2}\right) = -\log(f) + \log(A)$

(6) $\mathrm{y} = \mathrm{ax} + \mathrm{b}, \text{where } \mathrm{y} = \log\left(\frac{S_I}{I^2}\right),\ \mathrm{a} = -1,\ \mathrm{x} = \log(f),\ \mathrm{b} = \log(A)$

(7) $A = 10^{\mathrm{b}}$

(8) $\mathrm{SE}_A = 10^{\mathrm{b}} \cdot ln(10) \cdot \mathrm{SE}_b$

(9) $\mathrm{y} = \mathrm{be}^{\mathrm{ax}}, \text{where } \mathrm{y} = \mathrm{A}, \mathrm{a} = \gamma_3 \text{ or } \gamma_4,\ \mathrm{x} = \mathrm{d}$

(10) $\ln(\mathrm{y}) = \mathrm{ax} + \ln(\mathrm{b}), \text{where } \mathrm{y} = \mathrm{A},\ \mathrm{a} = \gamma_3 \text{ or } \gamma_4,\ \mathrm{x} = \mathrm{d}$

(11) $X = \frac{\mathrm{b}_2 - \mathrm{b}_1}{\mathrm{a}_1 - \mathrm{a}_2}$

(12) $\ln(Y) = \mathrm{a}_1 X + \mathrm{b}_1 = \mathrm{a}_2 X + \mathrm{b}_2$

(13) $\mathrm{SE}_X = \frac{1}{|\mathrm{a}_1 - \mathrm{a}_2|}\sqrt{X^2\left(\mathrm{SE}_{\mathrm{a}_1}^2 + \mathrm{SE}_{\mathrm{a}_2}^2\right) + \mathrm{SE}_{\mathrm{b}_1}^2 + \mathrm{SE}_{\mathrm{b}_2}^2}$

(14) $SE_{Y,ln} = \frac{1}{|\mathrm{a}_1 - \mathrm{a}_2|}\sqrt{X^2\left(\mathrm{a}_2^2 \cdot \mathrm{SE}_{\mathrm{a}_1}^2 + \mathrm{a}_1^2 \cdot \mathrm{SE}_{\mathrm{a}_2}^2\right) + \mathrm{a}_2^2 \cdot \mathrm{SE}_{\mathrm{b}_1}^2 + \mathrm{a}_1^2 \cdot \mathrm{SE}_{\mathrm{b}_2}^2}$

(15) $Y = \mathrm{e}^{\mathrm{a}_1 X + \mathrm{b}_1}$

(16) $\mathrm{SE}_Y = Y \cdot \mathrm{SE}_{Y,ln}$

5.6 Supporting information

5.6.1 Graphene sample preparation and nanopore fabrication

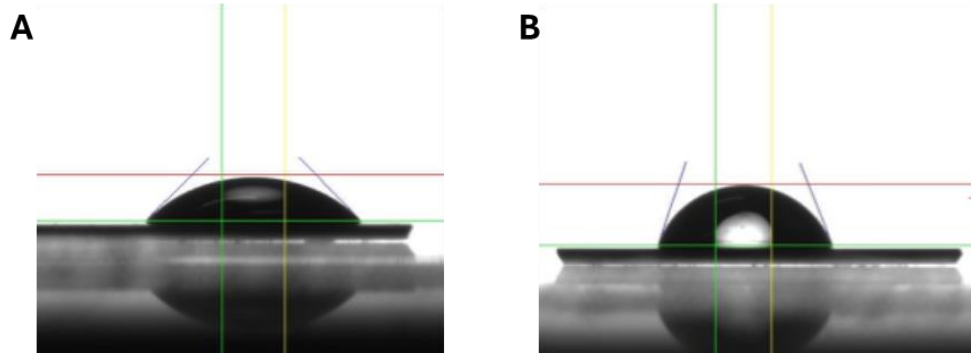

Figure S5.1 Contact angle measurements of SiNx chips after APTES and pyrene functionalization. (A) Example contact angle measurement after APTES functionalization. (B) Example contact angle measurement after pyrene functionalization.

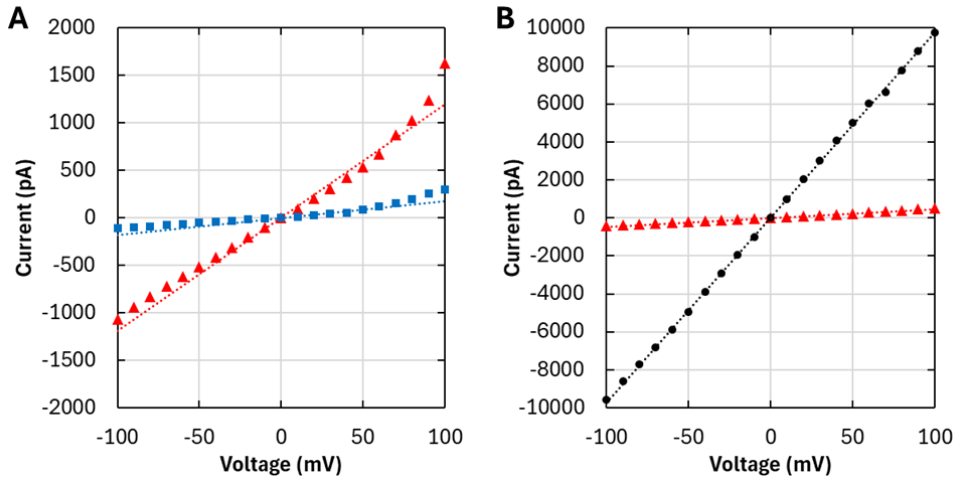

Figure S5.2 I-V measurements of sample 44 on a SiNx chip with 500 nm aperture diameter during before and after pore nucleation and pore enlargement processes. (A) I-V measurement of graphene transferred onto the SiNx chip before nucleation (blue squares) and after nucleation (red triangles) in 3.6 M NaCl + 10 µM HEPES. (B) I-V measurement of graphene nanopore before enlargement (red triangles) and after enlargement (black dots) in 1.0 M NaCl + 10 µM HEPES.

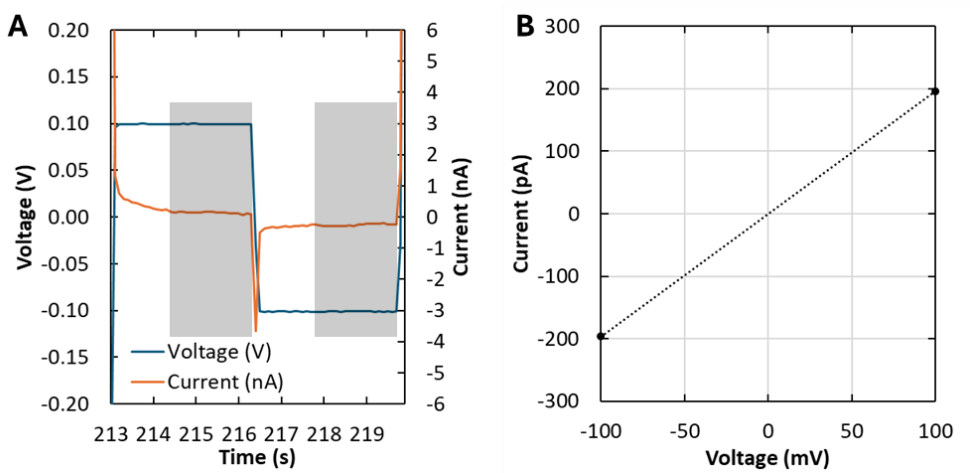

Figure S5.3 Example of a quick measure process for sample 2 on a SiNx chip with 100 nm aperture diameter in 1.0 mM NaCl + 10 µM HEPES. (A) Zoom in of a quick measure in between two blocks of pulse cycles during pore enlargement (green block in Figure 5.3B). A voltage of +100 mV and -100 mV was applied for 3 s consecutively, and the current values of the last two seconds at each voltage were recorded (gray blocks). (B) The average values of these currents (in pA) were plotted against the voltage (in mV) to obtain a rapid, rough estimation of the conductance.

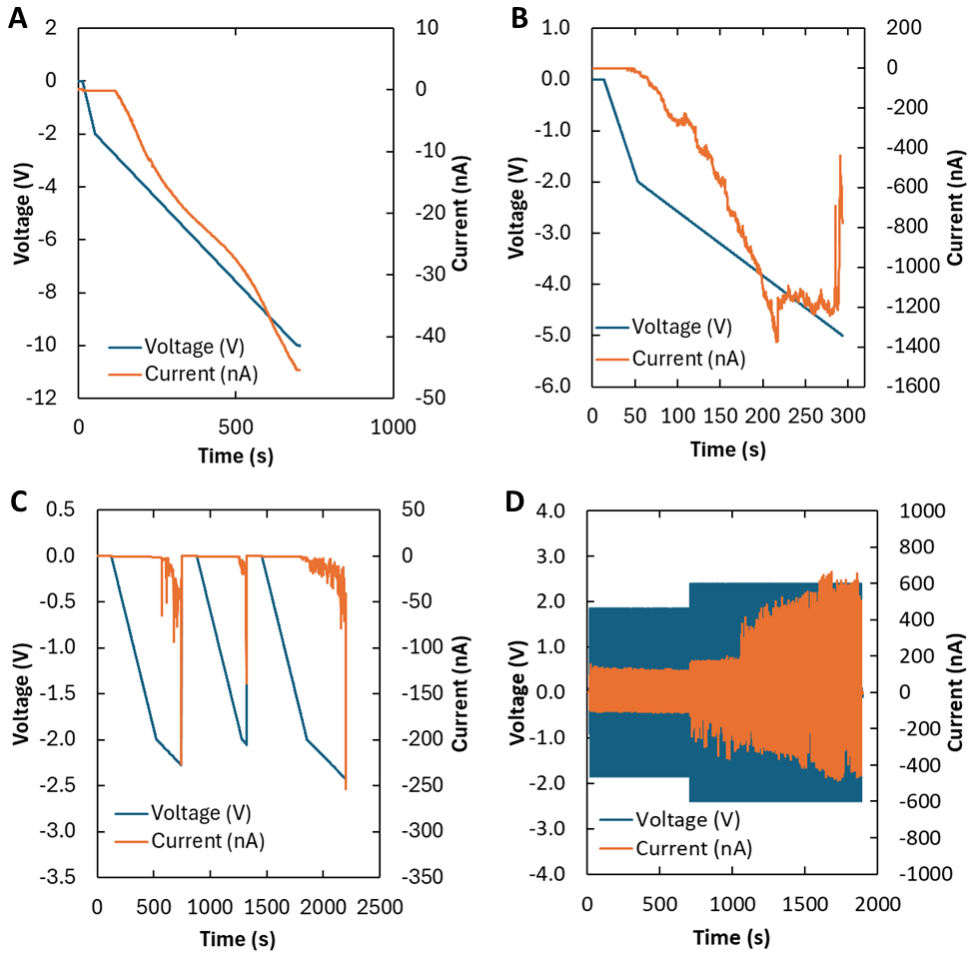

Figure S5.4 Several encountered problems during pore nucleation process on 500 nm free-standing graphene films in 3.6 M NaCl + 10 µM HEPES. (A) Absence of pore nucleation up to -10 V. (B) Premature termination of pore nucleation due to instability in current. (C) False breakdown events leading to insignificant conductance values (G < 0.3 nS). (D) Continuing to pore enlargement after false breakdown could still lead to increase in pore conductance, as observed by the larger current with increasing time.

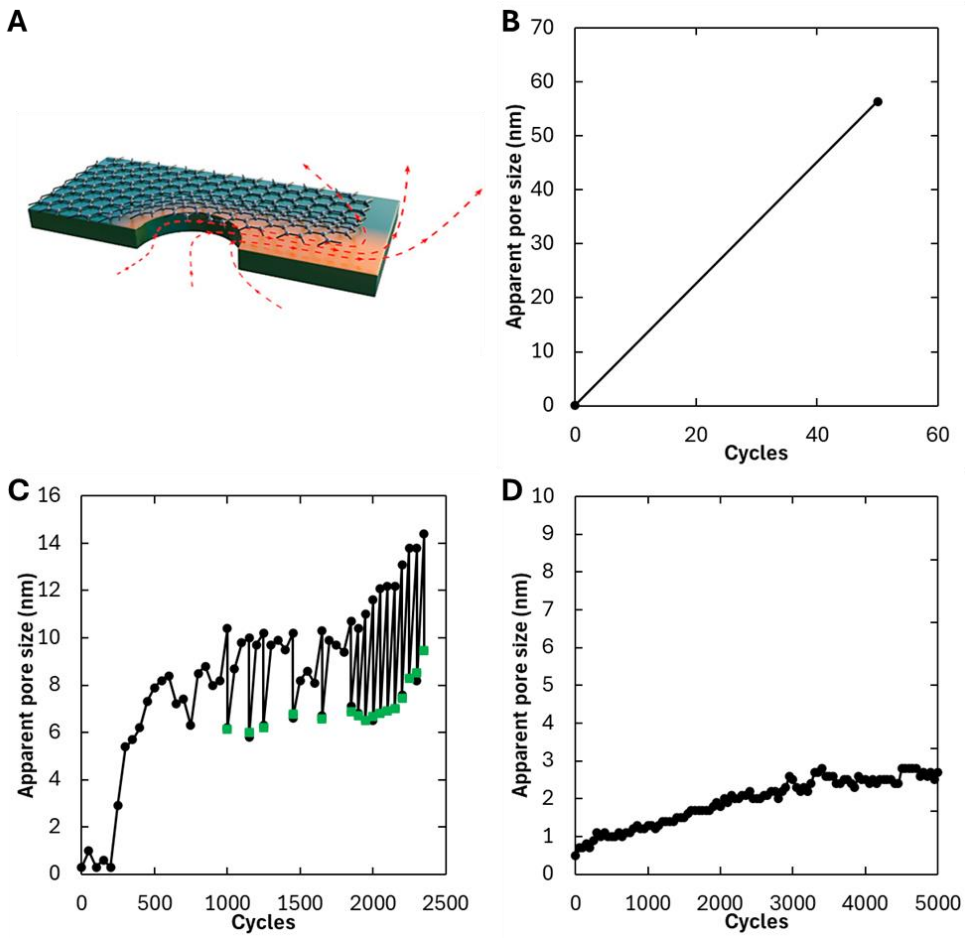

Figure S5.5 Several encountered problems during pore enlargement process on 500 nm free-standing graphene films in 1.0 M NaCl + 10 µM HEPES. (A) Voltage mediated delamination (VMD) is a reversible phenomenon that allows ions to bypass the graphene membrane when a high voltage potential is applied.[51] (B) Sudden increase in pore size during pore enlargement. (C) Overestimation of pore size during quick measures. When the calculated pore size from the quick measure (black dots) exceeded 10 nm according to Equation (1), I-V measurements (green squares) were automatically performed to obtain a more accurate value of the pore size (see Table S5.9). When the calculated pore size from the I-V measurements was not close to the target 10 nm, the enlargement process is continued. (D) Very slow pore enlargement at enlargement values equal to 100% of the pore nucleation voltage.

Table S5.1 Experimental results and controlled breakdown parameters for graphene nanopore nucleation.

Sample	Aperture diameter	Nucleation buffer [a]	Nucleation voltage (V)	Nucleated pore size (nm)
1	100 nm	1.0 M NaCl	4.1	1.79
2	100 nm	1.0 M NaCl	2.2	0.06
3	100 nm	1.0 M NaCl	2.3	1.61
4	100 nm	3.6 M NaCl	4.5	0.26
5	100 nm	3.6 M NaCl	3.9	2.54
6	100 nm	3.6 M NaCl	3.1	1.89
7	100 nm	3.6 M NaCl	3.3	0.70
8	100 nm	3.6 M NaCl	3.9	1.89
9	100 nm	3.6 M NaCl	2.5	0.70
10	500 nm	3.6 M NaCl	2.3	0.08
11	500 nm	3.6 M NaCl	2.5	0.55
12	500 nm	3.6 M NaCl	3.3	0.05
13	500 nm	3.6 M NaCl	2.3	0.08
14	500 nm	3.6 M NaCl	2.0	0.90
15	500 nm	3.6 M NaCl	3.0	0.25
16	500 nm	3.6 M NaCl	2.1	0.08
17	500 nm	3.6 M NaCl	2.0	0.15
18	500 nm	3.6 M NaCl	1.8	0.09
19	500 nm	3.6 M NaCl	2.2	0.32
20	500 nm	3.6 M NaCl	2.9	0.62
21	500 nm	3.6 M NaCl	2.8	0.16
22	500 nm	3.6 M NaCl	2.1	0.36
23	500 nm	3.6 M NaCl	2.1	2.29
24	500 nm	3.6 M NaCl	2.4	0.52
25	500 nm	3.6 M NaCl	1.9	1.06
26	500 nm	3.6 M NaCl	2.8	0.05
27	500 nm	3.6 M NaCl	2.7	0.33
28	500 nm	3.6 M NaCl	2.3	1.88
29	500 nm	3.6 M NaCl	2.8	0.15
30	500 nm	3.6 M NaCl	2.0	0.15
31	500 nm	3.6 M NaCl	2.0	1.14
32	500 nm	3.6 M NaCl	2.1	0.08
33	500 nm	3.6 M NaCl	2.0	0.65
34	500 nm	3.6 M NaCl	2.8	2.92
35	500 nm	3.6 M NaCl	2.2	0.09
36	500 nm	3.6 M NaCl	2.5	0.40
37	500 nm	3.6 M NaCl	2.6	0.24
38	500 nm	3.6 M NaCl	2.7	0.22
39	500 nm	3.6 M NaCl	2.2	0.14
40	500 nm	3.6 M NaCl	2.0	0.70
41	500 nm	3.6 M NaCl	2.2	0.73

42	500 nm	3.6 M NaCl	3.2	0.07
43	500 nm	3.6 M NaCl	2.8	0.33
44	500 nm	3.6 M NaCl	2.2	2.67
45	500 nm	3.6 M NaCl	2.7	0.48
46	500 nm	1.0 M NaCl + 10 μM SDS	2.0	0.06
47	500 nm	1.0 M NaCl + 10 μM SDS	2.2	0.21
48	500 nm	1.0 M NaCl + 10 μM SDS	2.9	0.72
49	500 nm	1.0 M NaCl + 10 μM SDS	2.5	0.14
50	500 nm	1.0 M NaCl + 10 μM SDS	2.6	0.11
51	500 nm	3.6 M NaCl + 10 μM SDS	2.4	0.23
52	500 nm	3.6 M NaCl + 10 μM SDS	2.9	0.17
53	500 nm	3.6 M NaCl	2.0	5.71
54	500 nm	3.6 M NaCl	4.6	8.64
55	500 nm	3.6 M NaCl	3.6	10.60
56	500 nm	3.6 M NaCl	2.3	4.89
57	500 nm	3.6 M NaCl + 10 μM SDS	4.0	9.15

[a] All buffers include 10 mM HEPES.

Table S5.2 Overall experimental results for the nucleation process in graphene nanopore fabrication.

Number of samples	Aperture diameter	Nucleation buffer [a]	Average nucleation voltage (V) [b]	Average nucleated pore size (nm) [b]
3	100 nm	1.0 M NaCl	-2.9 ± 0.7	1.2 ± 0.7
6	100 nm	3.6 M NaCl	-3.5 ± 0.3	1.3 ± 0.4
36	500 nm	3.6 M NaCl	-2.4 ± 0.1	0.6 ± 0.1
5	500 nm	1.0 M NaCl + 10 μM SDS	-2.4 ± 0.2	0.3 ± 0.1
2	500 nm	3.6 M NaCl + 10 μM SDS	-2.6 ± 0.3	0.2 ± 0.05

[a] All buffers include 10 mM HEPES.

[b] The errors represent the standard errors.

Table S5.3 Experimental results and controlled breakdown parameters for graphene nanopore enlargement.

Sample	Enlargement buffer [a]	Enlargement voltage (V)	Enlargement efficiency (cycles nm^{-1})
1	1.0 M NaCl	2.02	151
2	1.0 M NaCl	1.46	467
3	1.0 M NaCl	1.38	66
4	1.0 M NaCl	3.14	255
5	1.0 M NaCl	1.95	1018
6	1.0 M NaCl	2.97	812
7	1.0 M NaCl	3.09	- [b]
8	3.6 M NaCl	2.33	461
9	3.6 M NaCl	2.26	1913
10	1.0 M NaCl	1.82	303
11	1.0 M NaCl	1.77	107
12	1.0 M NaCl	2.04	477
13	1.0 M NaCl	2.39	354
14	1.0 M NaCl	2.29	1826
15	1.0 M NaCl	1.82	130
16	1.0 M NaCl	1.49	1884
17	1.0 M NaCl	1.60	1788
18	1.0 M NaCl	1.47	1725
19	1.0 M NaCl	1.98	2334
20	1.0 M NaCl	1.85	130
21	1.0 M NaCl	1.85	14
22	1.0 M NaCl	1.85	34
23	1.0 M NaCl	1.85	26
24	1.0 M NaCl	1.85	61
25	1.0 M NaCl	1.85	146
26	1.0 M NaCl	1.85	93
27	1.0 M NaCl	1.85	63
28	1.0 M NaCl	1.85	67
29	1.0 M NaCl	1.85	239
30	1.0 M NaCl	1.85	41
31	1.0 M NaCl	1.85	217
32	1.0 M NaCl	1.85	29
33	1.0 M NaCl	1.85	565
34	1.0 M NaCl	1.85	31
35	1.0 M NaCl	1.85	- [c]
36	1.0 M NaCl	2.39	- [c]
37	1.0 M NaCl	1.85	- [c]
38	1.0 M NaCl	1.85	- [c]
39	1.0 M NaCl	1.85	- [c]
40	1.0 M NaCl	1.85	- [c]
41	1.0 M NaCl	1.85	- [c]

42	1.0 M NaCl	2.00	- [d]
43	1.0 M NaCl	2.00	- [d]
44	1.0 M NaCl	2.00	- [d]
45	1.0 M NaCl	2.13	- [d]
46	1.0 M NaCl + 10 µM SDS	1.56	422
47	1.0 M NaCl + 10 µM SDS	1.43	249
48	1.0 M NaCl + 10 µM SDS	1.85	57
49	1.0 M NaCl + 10 µM SDS	1.85	17
50	1.0 M NaCl + 10 µM SDS	1.85	65
51	1.0 M NaCl + 10 µM SDS	1.50	8.9
52	1.0 M NaCl + 10 µM SDS	2.29	- [d]
53	1.0 M NaCl	1.85	- [c]
54	1.0 M NaCl + 10 µM SDS	2.27	- [c]
55	not performed	not performed	not performed
56	1.0 M NaCl	1.85	- [c]
57	1.0 M NaCl + 10 µM SDS	1.00	- [c]

[a] All buffers include 10 mM HEPES.

[b] could not enlarge.

[c] overshot enlargement.

[d] pulse durations 0.2 – 0.5 s during enlargement.

Table S5.4 Overall experimental results for the enlargement process in graphene nanopore fabrication.

Number of samples	Aperture size chip	Enlargement buffer [a]	Average enlargement voltage (V) [b]	Average enlargement efficiency (cycles nm^{-1}) [b]
6	100 nm	1.0 M NaCl	-2.2 ± 0.3	$4.6 \pm 1.7 \times 10^{2}$
2	100 nm	3.6 M NaCl	-2.3 ± 0.1	$1.2 \pm 1.0 \times 10^{3}$
10	500 nm	1.0 M NaCl	-1.9 ± 0.1	$1.1 \pm 0.3 \times 10^{3}$
15	500 nm	1.0 M NaCl	-1.85 [c]	$1.2 \pm 0.3 \times 10^{2}$ [c]
4	500 nm	1.0 M NaCl + 10 µM SDS	-1.5 ± 0.04	$2.3 \pm 1.5 \times 10^{2}$
3	500 nm	1.0 M NaCl + 10 µM SDS	-1.85 [c]	46 ± 18 [c]

[a] All buffers include 10 mM HEPES.
[b] The errors represent the standard errors.
[c] A static enlargement voltage of 1.85 V was applied.

Table S5.5 Pore conductance and 1/*f* noise amplitude of graphene nanopores fabricated by controlled breakdown before coating (bare) and after PPEG coating.

Sample	G_{bare} (nS)	A_{bare} [a]	G_{PPEG} (nS)	A_{PPEG} [a]	*N*	Individual pore diameter (nm) [e]
15 [b]	40	$3.18 \pm 2.56 \times 10^{-5}$	23	$4.95 \pm 3.67 \times 10^{-4}$	1	5.80
19 [b]	58	$1.64 \pm 1.24 \times 10^{-5}$	55	$2.69 \pm 1.83 \times 10^{-3}$	1 [d]	10.7
41 [b]	44	$5.79 \pm 4.06 \times 10^{-5}$	5.5	$1.63 \pm 1.07 \times 10^{-3}$	19	0.65
46 [c]	22	$3.49 \pm 2.61 \times 10^{-4}$	1.1	$4.23 \pm 2.58 \times 10^{-3}$	23	0.38
47 [c]	33	$1.31 \pm 0.93 \times 10^{-3}$	9.0	$1.35 \pm 1.07 \times 10^{-3}$	4	1.60

[a] The errors were propagated from the standard errors of the coefficients obtained *via* LINEST analysis (see methods section).
[b] Samples were measured in 1.0 M NaCl + 10 mM HEPES.
[c] Samples were measured in 1.0 M NaCl + 10 mM HEPES + 10 µM SDS.
[d] Includes assumption that PPEG coating effect on conductance was masked by the unclogging/damage
[e] Includes assumption that all pores are evenly distributed in size

5.6.2 TEM measurements of graphene membrane after controlled breakdown

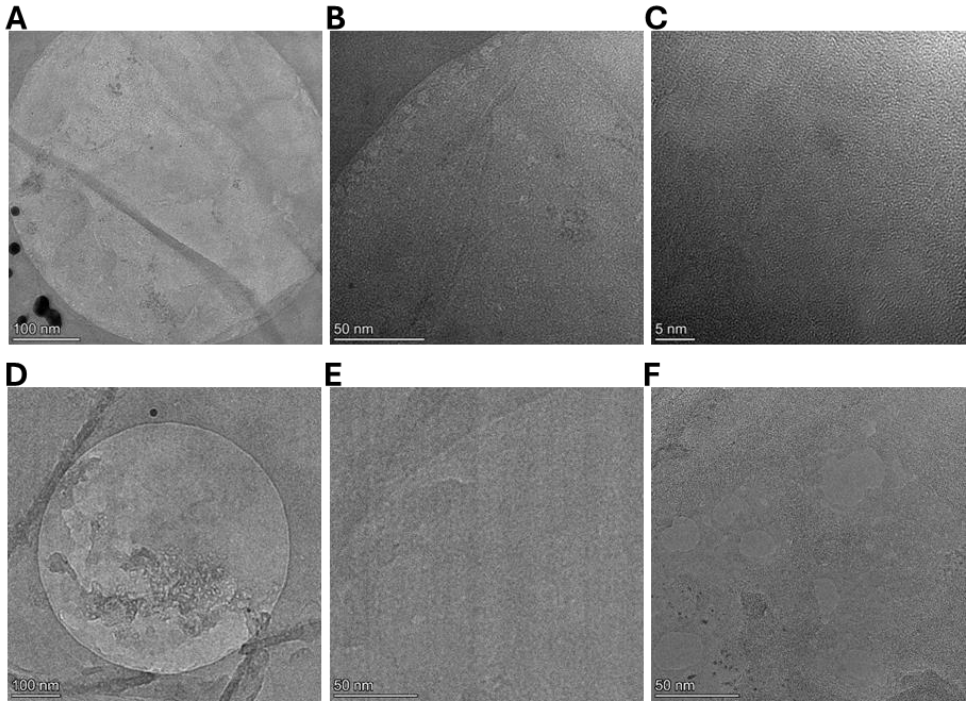

Figure S5.6 Transmission electron microscopy (TEM) images of graphene membranes after controlled breakdown. (A-C) Sample **57** imaged at 80 kV acceleration voltage at different magnifications. (D-F) Sample **56** imaged at 300 kV acceleration voltage at different magnifications. (F) After longer exposure times, holes started to form in the graphene membrane.

5.6.3 Pore stability of graphene nanopores fabricated by CBD

Table S5.6 Pore conductance of graphene nanopores over time and after flushing.

Sample	$Buffer_{start}$	G_{start} (nS) [a]	G_{wait} (nS, waiting time) [a]	G_{flush} (nS, number of flushes) [b]	G_{SDS} (nS) [c]	G_{NaCl} (nS) [d]
6	1.0 M NaCl	68	67 (10 min)	65 (after 9 flushes)	68	67
14	1.0 M NaCl	54	50 (10 min)	n.d.	52	29
15	M NaCl	60	n.d.	n.d.	64	64
22	3.6 M NaCl	153	143 (30 min)	n.d.	n.d.	n.d.
23	3.6 M NaCl	162	129 (20 min)	n.d.	n.d.	n.d.
24	3.6 M NaCl	201	195 (20 min)	n.d.	n.d.	n.d.
32	1.0 M NaCl	80	78 (10 min)	43 (after 9 flushes)	n.d.	n.d.
34	1.0 M NaCl	26	19 (10 min)	n.d.	14	n.d.
42	1.0 M NaCl	58	54 (10 min)	n.d.	n.d.	n.d.
43	1.0 M NaCl	53	49 (6 min)	n.d.	n.d.	n.d.
44	1.0 M NaCl	97	58 (210 min)	n.d.	59	n.d.
45	1.0 M NaCl	66	43 (195 min)	32 (after 2 flushes)	n.d.	n.d.
48	1.0 M NaCl + 10 µM SDS	68	n.d.	65 (after 2 flushes)	54	65
49	1.0 M NaCl + 10 µM SDS	76	n.d.	61 (after 2 flushes)	53	48
52	1.0 M NaCl + 10 µM SDS	100	94 (116 min)	n.d.	n.d.	n.d.
53	1.0 M NaCl	114	105 (10 min)	n.d.	105	95
54	1.0 M NaCl + 10 µM SDS	128	n.d.	128 (after 2 flushes)	122	116
55 [e]	3.6 M NaCl	171	197 (20 min)	n.d.	n.d.	n.d.
57	1.0 M NaCl + 10 µM SDS	122	105 (15 min)	99 (after 2 flushes)	n.d.	n.d.

n.d. not determined

[a] Samples were submerged and measured in $buffer_{start}$, which include 10 mM HEPES.

[b] Samples were flushed and measured in 1.0 M NaCl + 10 mM HEPES.

[c] Samples were flushed and measured in 1.0 M NaCl + 10 mM HEPES + 10 µM SDS.

[d] After measuring G_{SDS}, samples were flushed and measured in 1.0 M NaCl + 10 mM HEPES.

[e] Sample was fabricated using only pore nucleation without any pore enlargement.

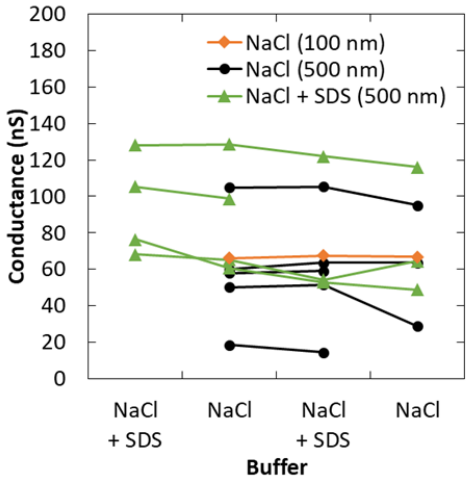

Figure S5.7 Conductance (in nS) before and after flushing with 1.0 M NaCl + 10 mM HEPES (NaCl) and 1.0 M NaCl + 10 mM HEPES + 10 µM (NaCl + SDS). Orange diamonds represent samples on a SiNx chip with 100 nm aperture diameter fabricated without the presence of SDS. Black dots represent samples on SiNx chip with 500 nm aperture diameter fabricated without the presence of SDS. Green triangles represent samples on SiNx chip with 500 nm aperture diameter fabricated in the presence of SDS. The results are listed in Table S5.6.

5.6.4 Noise of graphene nanopores fabricated by CBD

Table S5.7 Noise analysis of graphene nanopores fabricated by controlled breakdown.

Sample	Aperture diameter	Buffer [a]	A [b]	d (nm) [c]	R (MΩ)
1	100 nm	1.0 M NaCl	$2.54 \pm 2.08 \times 10^{-5}$	9.4	16.1
2	100 nm	1.0 M NaCl	$1.01 \pm 0.83 \times 10^{-5}$	10.7	14.1
3	100 nm	1.0 M NaCl	$1.69 \pm 1.23 \times 10^{-4}$	7.6	20.3
4	100 nm	1.0 M NaCl	$1.44 \pm 1.15 \times 10^{-4}$	7.6	20.3
5	100 nm	1.0 M NaCl	$1.12 \pm 0.77 \times 10^{-5}$	9.2	16.6
6	100 nm	1.0 M NaCl	$9.40 \pm 6.99 \times 10^{-7}$	9.4	14.8
7	100 nm	1.0 M NaCl	$2.77 \pm 2.30 \times 10^{-6}$	3.3	47.7
10	500 nm	1.0 M NaCl	$6.81 \pm 5.83 \times 10^{-5}$	9.4	16.2
11	500 nm	1.0 M NaCl	$9.01 \pm 6.46 \times 10^{-5}$	10.4	14.5
12	500 nm	1.0 M NaCl	$7.95 \pm 5.71 \times 10^{-5}$	6.8	21.0
13	500 nm	1.0 M NaCl	$1.36 \pm 1.11 \times 10^{-6}$	12.4	11.0
14	500 nm	1.0 M NaCl	$3.55 \pm 2.21 \times 10^{-7}$	7.6	18.5
15	500 nm	1.0 M NaCl	$3.18 \pm 2.56 \times 10^{-5}$	8.3	17.0
16	500 nm	1.0 M NaCl	$2.27 \pm 1.73 \times 10^{-4}$	4.6	32.3
17	500 nm	1.0 M NaCl	$1.17 \pm 0.82 \times 10^{-5}$	7.2	19.7
18	500 nm	1.0 M NaCl	$5.95 \pm 4.77 \times 10^{-4}$	3.2	50.6
19	500 nm	1.0 M NaCl	$1.64 \pm 1.24 \times 10^{-5}$	8.2	17.3

20	500 nm	1.0 M NaCl	$1.26 \pm 0.80 \times 10^{-4}$	7.4	21.0
21	500 nm	1.0 M NaCl	$1.28 \pm 0.90 \times 10^{-4}$	14.5	10.2
26	500 nm	1.0 M NaCl	$4.52 \pm 3.14 \times 10^{-5}$	8.4	18.1
27	500 nm	1.0 M NaCl	$3.51 \pm 2.62 \times 10^{-5}$	9.0	17.0
29	500 nm	1.0 M NaCl	$3.65 \pm 2.48 \times 10^{-5}$	8.0	19.2
32	500 nm	1.0 M NaCl	$1.27 \pm 0.97 \times 10^{-4}$	11.0	12.5
33	500 nm	1.0 M NaCl	$1.21 \pm 0.89 \times 10^{-4}$	7.7	18.4
34	500 nm	1.0 M NaCl	$7.72 \pm 5.63 \times 10^{-4}$	4.0	38.3
41	500 nm	1.0 M NaCl	$5.79 \pm 4.06 \times 10^{-5}$	15.3	8.8
42	500 nm	1.0 M NaCl	$2.28 \pm 2.00 \times 10^{-4}$	8.2	17.1
43	500 nm	1.0 M NaCl	$4.79 \pm 3.37 \times 10^{-4}$	7.5	19.0
44	500 nm	1.0 M NaCl	$1.53 \pm 1.04 \times 10^{-4}$	13.2	10.3
45	500 nm	1.0 M NaCl	$1.44 \pm 1.08 \times 10^{-3}$	9.2	15.1
53	500 nm	1.0 M NaCl	$9.87 \pm 7.41 \times 10^{-7}$	15.5	8.8
46	nm	1.0 M NaCl + 10 µM SDS	$3.49 \pm 2.61 \times 10^{-4}$	3.9	40.3
47	500 nm	1.0 M NaCl + 10 µM SDS	$1.31 \pm 0.93 \times 10^{-3}$	4.9	30.5
48	500 nm	1.0 M NaCl + 10 µM SDS	$7.17 \pm 4.52 \times 10^{-4}$	10.9	12.7
49	500 nm	1.0 M NaCl + 10 µM SDS	$4.31 \pm 3.38 \times 10^{-4}$	11.1	12.6
50	500 nm	1.0 M NaCl + 10 µM SDS	$1.61 \pm 1.23 \times 10^{-5}$	10.6	13.1
52	500 nm	1.0 M NaCl + 10 µM SDS	$4.51 \pm 3.49 \times 10^{-5}$	13.8	10.0
51	500 nm	1.0 M NaCl + 10 µM SDS	$1.07 \pm 0.79 \times 10^{-5}$	10.3	13.5
8	100 nm	3.6 M NaCl	$8.85 \pm 6.71 \times 10^{-5}$	5.5	10.9
9	100 nm	3.6 M NaCl	$1.53 \pm 1.03 \times 10^{-5}$	6.3	9.5
22	500 nm	3.6 M NaCl	$1.08 \pm 0.80 \times 10^{-4}$	9.2	6.2
23	500 nm	3.6 M NaCl	$2.22 \pm 1.71 \times 10^{-5}$	9.3	6.2
24	500 nm	3.6 M NaCl	$7.60 \pm 5.25 \times 10^{-5}$	11.4	5.0
30	500 nm	3.6 M NaCl	$1.67 \pm 1.14 \times 10^{-5}$	9.5	6.0
55	500 nm	3.6 M NaCl	$1.27 \pm 0.91 \times 10^{-7}$	9.7	5.9

[a] All buffers include 10 mM HEPES.

[b] The errors were propagated from the standard errors of the coefficients obtained *via* LINEST analysis (see methods section).

[c] Hypothetical single pore diameters calculated from experimental conductance values according to Equation (1).

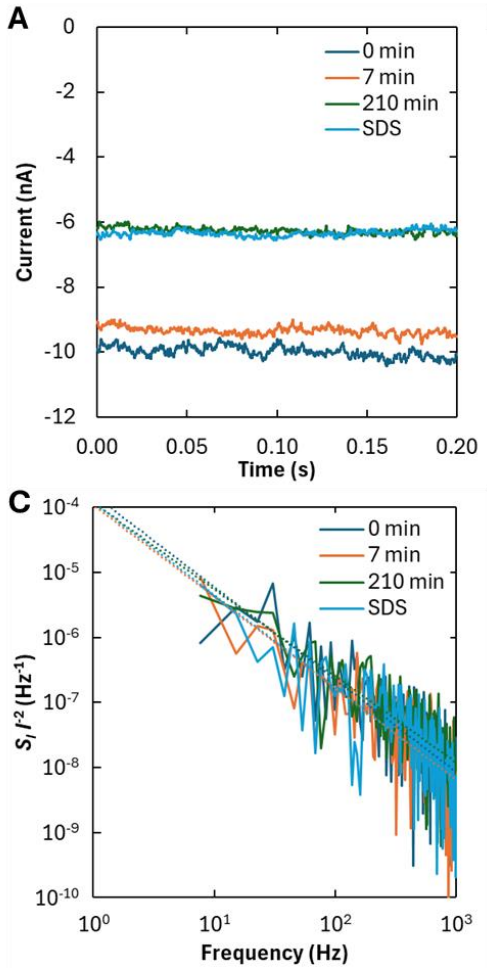

Figure S5.8 The 1/*f* noise dependency on time after fabrication and presence of SDS. (A) The current (in nA) plotted against time (in s) of sample 44 at different times after fabrication at a fixed bias voltage of -100 mV. The current traces were recorded in 1.0 M NaCl + 10 mM HEPES immediately after fabrication (dark blue line), 7 min after fabrication (orange line), and 210 min after fabrication (green line). After 210 min, the fluidic cell was flushed with 1.0 M NaCl + 10 mM HEPES + 10 μM SDS and a new current trace was recorded (light blue line). (B) The S_I (in pA^2 Hz^{-1}) plotted against frequency (in Hz) extracted from the current-time traces in panel A. (C) The normalized 1/*f* noise ($S_I I^{-2}$, in pA^2 Hz^{-1}) plotted against frequency (in Hz) extracted from panels A and B.

Table S5.8 Overall experimental results for the noise analysis in graphene nanopore fabrication.

Number of samples	Aperture diameter	Buffer [a]	A_{avg} [b]
7	100 nm	1.0 M NaCl	$1.5 \pm 1.6 \times 10^{-5}$
24	500 nm	1.0 M NaCl	$5.9 \pm 3.0 \times 10^{-5}$
7	500 nm	1.0 M NaCl + 10 µM SDS	$1.4 \pm 1.5 \times 10^{-4}$
2	100 nm	3.6 M NaCl	$3.7 \pm 5.2 \times 10^{-5}$
5	500 nm	3.6 M NaCl	$1.3 \pm 3.1 \times 10^{-5}$

[a] All buffers include 10 mM HEPES.

[b] The 1/*f* noise amplitude values were averaged in logarithmic space (see methods section). The errors represent the standard errors.

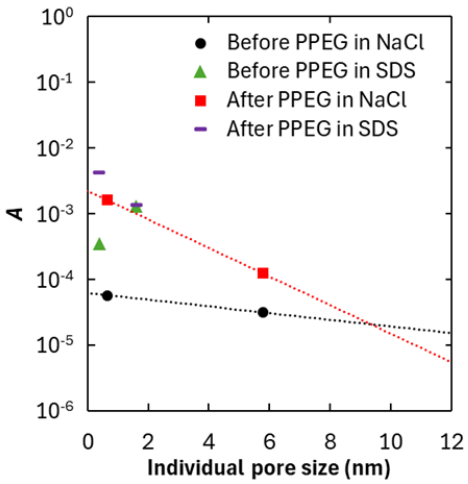

Figure S5.9 The values for *A* plotted against the individual pore size before and after PPEG coating. Black dots represent measurements before PPEG coating in 1.0 M NaCl + 10 mM HEPES. Green triangles represent measurements before PPEG coating in 1.0 M NaCl + 10 mM HEPES + 10 µM SDS. Red squares represent measurements after PPEG coating in 1.0 M NaCl + 10 mM HEPES. Purple dashes represent measurements after PPEG coating in 1.0 M NaCl + 10 mM HEPES + 10 µM SDS. The trendlines were obtained from linear regression in semi-logarithmic space (see methods section). List of samples and values can be found in Table S5.5.

Table S5.9 Nanopore fabrication protocols.ini

Conditioning.Fast Cond. Bias (V)=3
Conditioning.Conditioning Bias Max (V)=1.85
Conditioning.Measure Period (# of Cycles)=50
Conditioning.Pulse Width (s)=0.1
Conditioning.Fast/Slow So (% of target size)=80
Conditioning.Conditioning Bias Min (V)=-1.85
Conditioning.Intermediate 0 V State=FALSE
Conditioning.% of Breakdown V =50
Conditioning.% of Breakdown=TRUE
Fabrication.Starting Bias (V)=-2
Fabrication.Frequency (min)=10
Fabrication.Quick Measurement=FALSE
Fabrication.Threshold (nA)=2000
Fabrication.Fixed Threshold=TRUE
Fabrication.Ratio=1
Fabrication.Adaptive Threshold=TRUE
Fabrication.Med=50
Fabrication.Threshold (nm)=1
Fabrication.Ofs=125
Fabrication.Settling time (s)=0
Fabrication.Starting Bias Ramp (V/min)=-3
Fabrication.Maximum Bias Ramp (V/min)=-0.75
Fabrication.Maximum Bias (V)=-10
Fabrication.Fab Delay (s)=0
Fabrication.Cutoff (nA)=0
Quick Size Measurement.Bias (V)=0.1
Quick Size Measurement.Quick Wait Time (s)=1
Quick Size Measurement.Quick Measure Time (s)=2
Quick Size Measurement.Polarity=Positive+Negative
Size Measurement (I-V).Bias Max (V)=0.1
Size Measurement (I-V).Bias Min (V)=-0.1
Size Measurement (I-V).I-V Wait Time (s)=5
Size Measurement (I-V).I-V Measure Time (s)=2
Size Measurement (I-V).Number of Steps=11
Automation.Pre Tare Wait Time (s)=10
Automation.Final I-V Threshold (% of target)=90
Automation.L-Value Check=FALSE
Automation.Max L-Value=0.005
Automation.Max Pore Size=0
Automation.Single Side=FALSE

5.7 References

(1) Motone, K.; Kontogiorgos-Heintz, D.; Wee, J.; et al. Multi-Pass, Single-Molecule Nanopore Reading of Long Protein Strands. *Nature* **2024**, 1–8. https://doi.org/10.1038/s41586-024-07935-7.

(2) Olasagasti, F.; Lieberman, K. R.; Benner, S.; et al. Replication of Individual DNA Molecules under Electronic Control Using a Protein Nanopore. *Nat. Nanotechnol.* **2010**, *5* (11), 798–806. https://doi.org/10.1038/nnano.2010.177.

(3) Dorey, A.; Howorka, S. Nanopore DNA Sequencing Technologies and Their Applications towards Single-Molecule Proteomics. *Nat. Chem.* **2024**, *16* (3), 314–334. https://doi.org/10.1038/s41557-023-01322-x.

(4) Kasianowicz, J. J.; Robertson, J. W. F.; Chan, E. R.; et al. Nanoscopic Porous Sensors. *Annu. Rev. Anal. Chem.* **2008**, *1* (1), 737–766. https://doi.org/10.1146/annurev.anchem.1.031207.112818.

(5) Reiner, J. E.; Kasianowicz, J. J.; Nablo, B. J.; et al. Theory for Polymer Analysis Using Nanopore-Based Single-Molecule Mass Spectrometry. *Proc. Natl. Acad. Sci.* **2010**, *107* (27), 12080–12085. https://doi.org/10.1073/pnas.1002194107.

(6) Wang, Y.; Zhao, Y.; Bollas, A.; et al. Nanopore Sequencing Technology, Bioinformatics and Applications. *Nat. Biotechnol.* **2021**, *39* (11), 1348–1365. https://doi.org/10.1038/s41587-021-01108-x.

(7) Kowalczyk, S. W.; Hall, A. R.; Dekker, C. Detection of Local Protein Structures along DNA Using Solid-State Nanopores. *Nano Lett.* **2010**, *10* (1), 324–328. https://doi.org/10.1021/nl903631m.

(8) Cherf, G. M.; Lieberman, K. R.; Rashid, H.; et al. Automated Forward and Reverse Ratcheting of DNA in a Nanopore at 5-Å Precision. *Nat. Biotechnol.* **2012**, *30* (4), 344–348. https://doi.org/10.1038/nbt.2147.

(9) Manrao, E. A.; Derrington, I. M.; Laszlo, A. H.; et al. Reading DNA at Single-Nucleotide Resolution with a Mutant MspA Nanopore and Phi29 DNA Polymerase. *Nat. Biotechnol.* **2012**, *30* (4), 349–353. https://doi.org/10.1038/nbt.2171.

(10) Schneider, G. F.; Dekker, C. DNA Sequencing with Nanopores. *Nat. Biotechnol.* **2012**, *30* (4), 326–328. https://doi.org/10.1038/nbt.2181.

(11) Lenhart, B.; Wei, X.; Zhang, Z.; et al. Nanopore Fabrication and Application as Biosensors in Neurodegenerative Diseases. *Crit. Rev. Biomed. Eng.* **2020**, *48* (1), 29–62. https://doi.org/10.1615/CritRevBiomedEng.2020033151.

(12) Dekker, C. Solid-State Nanopores. *Nat. Nanotechnol.* **2007**, *2* (4), 209–215. https://doi.org/10.1038/nnano.2007.27.

(13) Merchant, C. A.; Healy, K.; Wanunu, M.; et al. DNA Translocation through Graphene Nanopores. *Nano Lett.* **2010**, *10* (8), 2915–2921. https://doi.org/10.1021/nl101046t.

(14) Schneider, G. F.; Kowalczyk, S. W.; Calado, V. E.; et al. DNA Translocation through Graphene Nanopores. *Nano Lett.* **2010**, *10* (8), 3163–3167. https://doi.org/10.1021/nl102069z.

(15) Garaj, S.; Hubbard, W.; Reina, A.; et al. Graphene as a Subnanometre Trans-Electrode Membrane. *Nature* **2010**, *467* (7312), 190–193. https://doi.org/10.1038/nature09379.

(16) Smeets, R. M. M.; Keyser, U. F.; Dekker, N. H.; et al. Noise in Solid-State Nanopores. *Proc. Natl. Acad. Sci.* **2008**, *105* (2), 417–421. https://doi.org/10.1073/pnas.0705349105.

(17) Yuan, Z.; Liu, Y.; Dai, M.; et al. Controlling DNA Translocation Through Solid-State Nanopores. *Nanoscale Res. Lett.* **2020**, *15* (1), 80. https://doi.org/10.1186/s11671-020-03308-x.
(18) Schneider, G. F.; Xu, Q.; Hage, S.; et al. Tailoring the Hydrophobicity of Graphene for Its Use as Nanopores for DNA Translocation. *Nat. Commun.* **2013**, *4* (1), 2619. https://doi.org/10.1038/ncomms3619.
(19) Yan, H.; Chen, T.; Hu, G.; et al. A Long-Term Stable Solid-State Nanopore for the Dynamic Monitoring of DNA Synthesis. *Anal. Chim. Acta* **2025**, *1344*, 343710. https://doi.org/10.1016/j.aca.2025.343710.
(20) Deng, T.; Li, M.; Wang, Y.; et al. Development of Solid-State Nanopore Fabrication Technologies. *Sci. Bull.* **2015**, *60* (3), 304–319. https://doi.org/10.1007/s11434-014-0705-8.
(21) Amaguayo, N.; Musello, A.; López, P.; et al. Fabrication of Nanopores Using the Controlled Dielectric Breakdown Technique. In *2021 IEEE Latin America Electron Devices Conference (LAEDC)*; **2021**; pp 1–4. https://doi.org/10.1109/LAEDC51812.2021.9437914.
(22) Kwok, H.; Briggs, K.; Tabard-Cossa, V. Nanopore Fabrication by Controlled Dielectric Breakdown. *PLOS ONE* **2014**, *9* (3), e92880. https://doi.org/10.1371/journal.pone.0092880.
(23) Arcadia, C. E.; Reyes, C. C.; Rosenstein, J. K. In Situ Nanopore Fabrication and Single-Molecule Sensing with Microscale Liquid Contacts. *ACS Nano* **2017**, *11* (5), 4907–4915. https://doi.org/10.1021/acsnano.7b01519.
(24) Yanagi, I.; Akahori, R.; Hatano, T.; et al. Fabricating Nanopores with Diameters of Sub-1 Nm to 3 Nm Using Multilevel Pulse-Voltage Injection. *Sci. Rep.* **2014**, *4* (1), 5000. https://doi.org/10.1038/srep05000.
(25) Zhou, Y.; Long, X.; Zhang, Y.; et al. Advances and Challenges in Solid-State Nanopores for DNA Sequencing. *Langmuir* **2025**, *41* (9), 5736–5761. https://doi.org/10.1021/acs.langmuir.4c04961.
(26) Yanagi, I.; Hamamura, H.; Akahori, R.; et al. Two-Step Breakdown of a SiN Membrane for Nanopore Fabrication: Formation of Thin Portion and Penetration. *Sci. Rep.* **2018**, *8* (1), 10129. https://doi.org/10.1038/s41598-018-28524-5.
(27) Xue, L.; Yamazaki, H.; Ren, R.; et al. Solid-State Nanopore Sensors. *Nat. Rev. Mater.* **2020**, *5* (12), 931–951. https://doi.org/10.1038/s41578-020-0229-6.
(28) Briggs, K.; Charron, M.; Kwok, H.; et al. Kinetics of Nanopore Fabrication during Controlled Breakdown of Dielectric Membranes in Solution. *Nanotechnology* **2015**, *26* (8), 084004. https://doi.org/10.1088/0957-4484/26/8/084004.
(29) Fried, J. P.; Swett, J. L.; Nadappuram, B. P.; et al. Understanding Electrical Conduction and Nanopore Formation During Controlled Breakdown. *Small* **2021**, *17* (37), 2102543. https://doi.org/10.1002/smll.202102543.
(30) van den Hout, M.; Hall, A. R.; Wu, M. Y.; et al. Controlling Nanopore Size, Shape and Stability. *Nanotechnology* **2010**, *21* (11), 115304. https://doi.org/10.1088/0957-4484/21/11/115304.
(31) Yanagi, I.; Akahori, R.; Takeda, K. Stable Fabrication of a Large Nanopore by Controlled Dielectric Breakdown in a High-pH Solution for the Detection of Various-Sized Molecules. *Sci. Rep.* **2019**, *9* (1), 13143. https://doi.org/10.1038/s41598-019-49622-y.

(32) Matsui, K.; Yanagi, I.; Goto, Y.; et al. Prevention of Dielectric Breakdown of Nanopore Membranes by Charge Neutralization. *Sci. Rep.* **2015**, *5* (1), 17819. https://doi.org/10.1038/srep17819.

(33) Goto, Y.; Matsui, K.; Yanagi, I.; et al. Silicon Nitride Nanopore Created by Dielectric Breakdown with a Divalent Cation: Deceleration of Translocation Speed and Identification of Single Nucleotides. *Nanoscale* **2019**, *11* (30), 14426–14433. https://doi.org/10.1039/C9NR03563J.

(34) Yanagi, I.; Akahori, R.; Takeda, K. Dwell Time Prolongation and Identification of Single Nucleotides Passing through a Solid-State Nanopore by Using Ammonium Sulfate Aqueous Solution. *ACS Omega* **2023**, *8* (23), 21285–21292. https://doi.org/10.1021/acsomega.3c02703.

(35) Feng, J.; Liu, K.; Graf, M.; et al. Electrochemical Reaction in Single Layer MoS2: Nanopores Opened Atom by Atom. *Nano Lett.* **2015**, *15* (5), 3431–3438. https://doi.org/10.1021/acs.nanolett.5b00768.

(36) Guo, H.-W.; Cui, Y.-J.; Zhang, Y.-Z.; et al. Stable Nanopores in Two-Dimensional Materials for Ion Conductivity Devices and Biosensors. *ACS Appl. Nano Mater.* **2022**, *5* (3), 3611–3618. https://doi.org/10.1021/acsanm.1c04270.

(37) Wang, Y.; Cheng, M.; Wang, L.; et al. Nanocrystalline Graphite Nanopores for DNA Sensing. *Carbon* **2021**, *176*, 271–278. https://doi.org/10.1016/j.carbon.2020.12.064.

(38) Crick, C. R.; Sze, J. Y. Y.; Rosillo-Lopez, M.; et al. Selectively Sized Graphene-Based Nanopores for in Situ Single Molecule Sensing. *ACS Appl. Mater. Interfaces* **2015**, *7* (32), 18188–18194. https://doi.org/10.1021/acsami.5b06212.

(39) Kuan, A. T.; Lu, B.; Xie, P.; et al. Electrical Pulse Fabrication of Graphene Nanopores in Electrolyte Solution. *Appl. Phys. Lett.* **2015**, *106* (20), 203109. https://doi.org/10.1063/1.4921620.

(40) Briggs, K.; Kwok, H.; Tabard-Cossa, V. Automated Fabrication of 2-Nm Solid-State Nanopores for Nucleic Acid Analysis. *Small* **2014**, *10* (10), 2077–2086. https://doi.org/10.1002/smll.201303602.

(41) Waugh, M.; Briggs, K.; Gunn, D.; et al. Solid-State Nanopore Fabrication by Automated Controlled Breakdown. *Nat. Protoc.* **2020**, *15* (1), 122–143. https://doi.org/10.1038/s41596-019-0255-2.

(42) Islam, M. F.; Yap, Y. C.; Li, F.; et al. The Influence of Electrolyte Concentration on Nanofractures Fabricated in a 3D-Printed Microfluidic Device by Controlled Dielectric Breakdown. *ELECTROPHORESIS* **2020**, *41* (23), 2007–2014. https://doi.org/10.1002/elps.202000050.

(43) Bello, J.; Shim, J. Solid-State Nanopore Fabrication in LiCl by Controlled Dielectric Breakdown. *Biomed. Microdevices* **2018**, *20* (2), 38. https://doi.org/10.1007/s10544-018-0281-9.

(44) Leung, C.; Briggs, K.; Laberge, M.-P.; et al. Mechanisms of Solid-State Nanopore Enlargement under Electrical Stress. *Nanotechnology* **2020**, *31* (44), 44LT01. https://doi.org/10.1088/1361-6528/aba86e.

(45) Ying, C.; Zhang, Y.; Feng, Y.; et al. 3D Nanopore Shape Control by Current-Stimulus Dielectric Breakdown. *Appl. Phys. Lett.* **2016**, *109* (6), 063105. https://doi.org/10.1063/1.4960636.

(46) Wang, Y.; Chen, Q.; Deng, T.; et al. Nanopore Fabricated in Pyramidal HfO2 Film by Dielectric Breakdown Method. *Appl. Phys. Lett.* **2017**, *111* (14), 143103. https://doi.org/10.1063/1.4990717.

(47) Carlsen, A. T.; Briggs, K.; Hall, A. R.; et al. Solid-State Nanopore Localization by Controlled Breakdown of Selectively Thinned Membranes. *Nanotechnology* **2017**, *28* (8), 085304. https://doi.org/10.1088/1361-6528/aa564d.

(48) Leva, C. V.; Jain, S.; Kistermann, K.; et al. Localized Nanopore Fabrication in Silicon Nitride Membranes by Femtosecond Laser Exposure and Subsequent Controlled Breakdown. *ACS Appl. Mater. Interfaces* **2025**, *17* (5), 8737–8748. https://doi.org/10.1021/acsami.5c00255.

(49) Chung, N. X.; Gatty, H. K.; Lu, X.; et al. Optimized Electrochemical Breakdown Etching Using Temporal Voltage Variation for Formation of Nanopores in a Silicon Membrane. *Sens. Actuators B Chem.* **2021**, *331*, 129323. https://doi.org/10.1016/j.snb.2020.129323.

(50) Kang, X.; Chen, B.; van Geest, E. P.; et al. Substrate-Tight Graphene Transmembrane-Nanofluidic Devices. *Small* **2025**, 2407140. https://doi.org/10.1002/smll.202407140.

(51) Loessberg-Zahl, J.; de Bruijn, D. S.; van den Beld, W. T. E.; et al. Exploring Voltage Mediated Delamination of Suspended 2D Materials as a Cause of Commonly Observed Breakdown. *J. Phys. Chem. C* **2020**, *124* (1), 430–435. https://doi.org/10.1021/acs.jpcc.9b08500.

(52) M. Eggenberger, O.; Ying, C.; Mayer, M. Surface Coatings for Solid-State Nanopores. *Nanoscale* **2019**, *11* (42), 19636–19657. https://doi.org/10.1039/C9NR05367K.

(53) Kowalczyk, S. W.; Grosberg, A. Y.; Rabin, Y.; et al. Modeling the Conductance and DNA Blockade of Solid-State Nanopores. *Nanotechnology* **2011**, *22* (31), 315101. https://doi.org/10.1088/0957-4484/22/31/315101.

(54) Paruchuri, V. K.; Nguyen, A. V.; Miller, J. D. Zeta-Potentials of Self-Assembled Surface Micelles of Ionic Surfactants Adsorbed at Hydrophobic Graphite Surfaces. *Colloids Surf. Physicochem. Eng. Asp.* **2004**, *250* (1), 519–526. https://doi.org/10.1016/j.colsurfa.2004.04.098.

(55) Chou, Y.-C.; Masih Das, P.; Monos, D. S.; et al. Lifetime and Stability of Silicon Nitride Nanopores and Nanopore Arrays for Ionic Measurements. *ACS Nano* **2020**, *14* (6), 6715–6728. https://doi.org/10.1021/acsnano.9b09964.

(56) Hu, R.; Tong, X.; Zhao, Q. Four Aspects about Solid-State Nanopores for Protein Sensing: Fabrication, Sensitivity, Selectivity, and Durability. *Adv. Healthc. Mater.* **2020**, *9* (17), 2000933. https://doi.org/10.1002/adhm.202000933.

(57) Lin, L.; Zhang, J.; Su, H.; et al. Towards Super-Clean Graphene. *Nat. Commun.* **2019**, *10* (1), 1912. https://doi.org/10.1038/s41467-019-09565-4.

(58) Zhuang, B.; Li, S.; Li, S.; et al. Ways to Eliminate PMMA Residues on Graphene — — Superclean Graphene. *Carbon* **2021**, *173*, 609–636. https://doi.org/10.1016/j.carbon.2020.11.047.

(59) Temiryazev, A.; Frolov, A.; Temiryazeva, M. Atomic-Force Microscopy Study of Self-Assembled Atmospheric Contamination on Graphene and Graphite Surfaces. *Carbon* **2019**, *143*, 30–37. https://doi.org/10.1016/j.carbon.2018.10.094.

(60) Li, Z.; Wang, Y.; Kozbial, A.; et al. Effect of Airborne Contaminants on the Wettability of Supported Graphene and Graphite. *Nat. Mater.* **2013**, *12* (10), 925–931. https://doi.org/10.1038/nmat3709.

(61) Zan, R.; Ramasse, Q. M.; Bangert, U.; et al. Graphene Reknits Its Holes. *Nano Lett.* **2012**, *12* (8), 3936–3940. https://doi.org/10.1021/nl300985q.

(62) Barreiro, A.; Börrnert, F.; Avdoshenko, S. M.; et al. Understanding the Catalyst-Free Transformation of Amorphous Carbon into Graphene by Current-Induced Annealing. *Sci. Rep.* **2013**, *3* (1), 1115. https://doi.org/10.1038/srep01115.

(63) Tsetseris, L.; Pantelides, S. T. Adatom Complexes and Self-Healing Mechanisms on Graphene and Single-Wall Carbon Nanotubes. *Carbon* **2009**, *47* (3), 901–908. https://doi.org/10.1016/j.carbon.2008.12.002.

(64) Lee, J.; Yang, Z.; Zhou, W.; et al. Stabilization of Graphene Nanopore. *Proc. Natl. Acad. Sci.* **2014**, *111* (21), 7522–7526. https://doi.org/10.1073/pnas.1400767111.

(65) Liu, Y.; Ma, Y.; Yang, J.; et al. Overcoming Chemical Stability Challenges of Nanoporous Graphene Separation Membranes in Harsh Environments. *Chem. Eng. J.* **2025**, *508*, 160721. https://doi.org/10.1016/j.cej.2025.160721.

(66) Fragasso, A.; Schmid, S.; Dekker, C. Comparing Current Noise in Biological and Solid-State Nanopores. *ACS Nano* **2020**, *14* (2), 1338–1349. https://doi.org/10.1021/acsnano.9b09353.

(67) Liang, S.; Xiang, F.; Tang, Z.; et al. Noise in Nanopore Sensors: Sources, Models, Reduction, and Benchmarking. *Nanotechnol. Precis. Eng.* **2020**, *3* (1), 9–17. https://doi.org/10.1016/j.npe.2019.12.008.

(68) Siwy, Z.; Fuliński, A. Origin of $1/f^{\alpha}$ Noise in Membrane Channel Currents. *Phys. Rev. Lett.* **2002**, *89* (15), 158101. https://doi.org/10.1103/PhysRevLett.89.158101.

(69) Tabard-Cossa, V.; Trivedi, D.; Wiggin, M.; et al. Noise Analysis and Reduction in Solid-State Nanopores. *Nanotechnology* **2007**, *18* (30), 305505. https://doi.org/10.1088/0957-4484/18/30/305505.

(70) Fragasso, A.; Pud, S.; Dekker, C. $1/f$ Noise in Solid-State Nanopores Is Governed by Access and Surface Regions. *Nanotechnology* **2019**, *30* (39), 395202. https://doi.org/10.1088/1361-6528/ab2d35.

(71) Uram, J. D.; Ke, K.; Mayer, M. Noise and Bandwidth of Current Recordings from Submicrometer Pores and Nanopores. *ACS Nano* **2008**, *2* (5), 857–872. https://doi.org/10.1021/nn700322m.

(72) Rosenstein, J. K.; Wanunu, M.; Merchant, C. A.; et al. Integrated Nanopore Sensing Platform with Sub-Microsecond Temporal Resolution. *Nat. Methods* **2012**, *9* (5), 487–492. https://doi.org/10.1038/nmeth.1932.

(73) Balandin, A. A. Low-Frequency $1/f$ Noise in Graphene Devices. *Nat. Nanotechnol.* **2013**, *8* (8), 549–555. https://doi.org/10.1038/nnano.2013.144.

(74) Kamada, M.; Zeng, W.; Laitinen, A.; et al. Suppression of $1/f$ Noise in Graphene Due to Anisotropic Mobility Fluctuations Induced by Impurity Motion. *Commun. Phys.* **2023**, *6* (1), 207. https://doi.org/10.1038/s42005-023-01321-x.

(75) Rehman, A.; Notario, J. A. D.; Sanchez, J. S.; et al. Nature of the $1/f$ Noise in Graphene—Direct Evidence for the Mobility Fluctuation Mechanism. *Nanoscale* **2022**, *14* (19), 7242–7249. https://doi.org/10.1039/D2NR00207H.

(76) Smeets, R. M. M.; Keyser, U. F.; Wu, M. Y.; et al. Nanobubbles in Solid-State Nanopores. *Phys. Rev. Lett.* **2006**, *97* (8), 088101. https://doi.org/10.1103/PhysRevLett.97.088101.

(77) Heerema, S. J.; Schneider, G. F.; Rozemuller, M.; et al. $1/f$ Noise in Graphene Nanopores. *Nanotechnology* **2015**, *26* (7), 074001. https://doi.org/10.1088/0957-4484/26/7/074001.

(78) Zhang, Z.-Y.; Deng, Y.-S.; Tian, H.-B.; et al. Noise Analysis of Monolayer Graphene Nanopores. *Int. J. Mol. Sci.* **2018**, *19* (9), 2639. https://doi.org/10.3390/ijms19092639.

(79) Chen, P.; Mitsui, T.; Farmer, D. B.; et al. Atomic Layer Deposition to Fine-Tune the Surface Properties and Diameters of Fabricated Nanopores. *Nano Lett.* **2004**, *4* (7), 1333–1337. https://doi.org/10.1021/nl0494001.

(80) Park, K.-B.; Kim, H.-J.; Kang, Y.-H.; et al. Highly Reliable and Low-Noise Solid-State Nanopores with an Atomic Layer Deposited ZnO Membrane on a Quartz Substrate. *Nanoscale* **2017**, *9* (47), 18772–18780. https://doi.org/10.1039/C7NR05755E.

(81) Beamish, E.; Kwok, H.; Tabard-Cossa, V.; et al. Precise Control of the Size and Noise of Solid-State Nanopores Using High Electric Fields. *Nanotechnology* **2012**, *23* (40), 405301. https://doi.org/10.1088/0957-4484/23/40/405301.

(82) Zhou, Z.; Hu, Y.; Wang, H.; et al. DNA Translocation through Hydrophilic Nanopore in Hexagonal Boron Nitride. *Sci. Rep.* **2013**, *3* (1), 3287. https://doi.org/10.1038/srep03287.

(83) Garaj, S.; Liu, S.; Golovchenko, J. A.; et al. Molecule-Hugging Graphene Nanopores. *Proc. Natl. Acad. Sci.* **2013**, *110* (30), 12192–12196. https://doi.org/10.1073/pnas.1220012110.

(84) Tadanaga, K.; Morinaga, J.; Matsuda, A.; et al. Superhydrophobic−Superhydrophilic Micropatterning on Flowerlike Alumina Coating Film by the Sol−Gel Method. *Chem. Mater.* **2000**, *12* (3), 590–592. https://doi.org/10.1021/cm990643h.

(85) Andryushchenko, V. A.; Sorokin, D. V.; Betke, I. A.; et al. Control of Graphene Adhesion to Substrate during Transfer through Liquid. *J. Mol. Liq.* **2024**, *395*, 123827. https://doi.org/10.1016/j.molliq.2023.123827.

(86) van Geest, E. P.; Can, B.; Makurat, M.; et al. Wafer-Scale Robust Graphene Electronics under Industrial Processing Conditions. arXiv January 22, **2025**. https://doi.org/10.48550/arXiv.2501.12963.